J. Fluid Mech. (2023), vol. 954, A28, doi:10.1017/jfm.2022.992

JFM PAPERS

Approximate streamsurfaces for flow visualization

Stergios Katsanoulis[1], **Florian Kogelbauer**[2], **Roshan Kaundinya**[1], **Jesse Ault**[3] **and George Haller**[1,†]

[1]Institute for Mechanical Systems, ETH Zurich, 8092 Zurich, Switzerland
[2]Department of Mechanical and Process Engineering, ETH Zurich, 8092 Zurich, Switzerland
[3]Center for Fluid Mechanics, School of Engineering, Brown University, Providence, RI 02912, USA

(Received 23 January 2022; revised 22 November 2022; accepted 22 November 2022)

Instantaneous features of three-dimensional velocity fields are most directly visualized via streamsurfaces. It is generally unclear, however, which streamsurfaces one should pick for this purpose, given that infinitely many such surfaces pass through each point of the flow domain. Exceptions to this rule are vector fields with a non-degenerate first integral whose level surfaces globally define a continuous, one-parameter family of streamsurfaces. While generic vector fields have no first integrals, their vortical regions may admit local first integrals over a discrete set of streamtubes, as Hamiltonian systems are known to do over Cantor sets of invariant tori. Here we introduce a method to construct such first integrals approximately from velocity data, and show that their level sets indeed frame vortical features of the velocity field in examples in which those features are known from Lagrangian analysis. Moreover, we test our method in numerical datasets, including a flow inside a V-junction and a turbulent channel flow. For the latter, we propound an algorithm to pin down the most salient barriers to momentum transport up to a given scale providing a way out of the occlusion conundrum that typically accompanies other vortex visualization methods.

Key words: vortex dynamics, turbulence theory, topological fluid dynamics

1. Introduction

Streamsurfaces of a three-dimensional flow are two-dimensional surfaces composed of streamlines. Even a small but judiciously chosen set of such surfaces can give an effective characterization of the global topology of the velocity field. In steady flows, streamsurfaces

---

† Email address for correspondence: georgehaller@ethz.ch

© The Author(s), 2023. Published by Cambridge University Press. This is an Open Access article, distributed under the terms of the Creative Commons Attribution licence (http://creativecommons.org/licenses/by/4.0), which permits unrestricted re-use, distribution and reproduction, provided the original article is properly cited.

are also invariant manifolds for the particle motion and hence frame the Lagrangian particle dynamics. For these reasons, streamsurfaces should be, in principle, the simplest tool for illustrating instantaneous features of a velocity field.

Analogously, to identify and visualize vortical features of a velocity field, Yang & Pullin (2010) generalized the notion of vortex tubes and sheets (Batchelor 2000) by defining the vortex-surface field (VSF), i.e. a smooth scalar field whose isosurfaces act as two-dimensional (2-D) invariant manifolds of the vorticity field. Initially developed for symmetric, inviscid flows (Yang & Pullin 2010), this work has been extended to capture approximations to the Lagrangian (material) evolution of VSFs in analytic viscous flows (Yang & Pullin 2011), shear flows (Xiong & Yang 2017), compressible flows (Peng & Yang 2018), transitional wall flows (Zhao, Yang & Chen 2016*a*,*b*) and in homogeneous isotropic turbulence (Xiong & Yang 2019). A different approach, based on the spherical Clebsch maps, was used by Chern *et al.* (2017) to visualize vortex lines and surfaces in computer graphics. However, neither VSFs nor streamsurfaces are objective (frame-indifferent; Haller 2005), which renders their experimental detection ambiguous.

In contrast, recent results on the transport of dynamically active vector fields (such as the momentum and vorticity fields) have yielded objectively defined barrier vector fields whose distinguished invariant surfaces turn out to be frame-indifferent material barriers to active transport (Haller *et al.* 2020). Specifically, the barrier vector fields are the velocity and vorticity Laplacian in the instantaneous (Eulerian) limit and the time-averaged pullbacks of these Laplacian fields in the Lagrangian case. The invariant manifolds of these barrier vector fields have been shown to highlight vortical features of the velocity field with increased accuracy in several 2-D and three-dimensional (3-D) flows (Haller *et al.* 2020; Aksamit & Haller 2022).

Irrespective of the underlying vector field, no general methodology is available for its efficient visualization via a well-placed set of invariant surfaces. This is because streamlines launched from any smooth curve form a streamsurface by definition. As a consequence, infinitely many streamsurfaces cross through any point of the flow domain. It is thus unclear which (if any) of these surfaces should be selected even locally as a representative of the vector field topology. As a consequence, flow visualization packages tend to rely on user input for seed points of streamlines and streamsurfaces.

Most related ongoing research in the scientific visualization community focuses either on the more accurate computation of streamsurfaces from select seed points (Hultquist 1992) or streamline selection for streamsurfaces based on visual optimization (Born *et al.* 2010; Schulze *et al.* 2014). A relatively recent realization is that the streamsurfaces framing the instantaneous flow behaviour most efficiently are the key invariant manifolds of the instantaneous velocity field. Local stable and unstable manifolds near stagnation points and closed streamlines indeed well illustrate the instantaneous local velocity field geometry (see, e.g. Peikert & Sadlo 2009) but generally stretch and fold globally. These globally filamented streamsurfaces then lose their ability to demarcate different flow regions efficiently, with unavoidable inaccuracies also arising in their computation (Sadlo & Peikert 2007). Closest in spirit to our work is the observation of Van Wijk (1993), who seeks streamsurfaces as level sets of a scalar function. After defining a scalar distribution within an inflow boundary, the level curves of this scalar field are propagated along streamlines into the flow. As a consequence, the resulting surfaces will generally stretch, fold and self-accumulate, resulting in filamenting streamsurfaces that also depend on the choice of the initial scalar distribution. Reviews of all these approaches in the scientific visualization community can be found, e.g. in Peikert & Sadlo (2009) and Martinez–Esturo *et al.* (2013).

A representative set of streamsurfaces for flow illustration should arguably include at least one surface for each typically observed streamline topology, as well as the (generally unobserved) surfaces separating these different topological classes. Finding such a set of streamlines is straightforward for 2-D incompressible flows by the existence of a first integral (conserved quantity) for the equation of instantaneous streamlines. This first integral is the streamfunction, whose set of level curves contains all typically observed streamline families as well as separatrices among them. Therefore, one can systematically scan through the one-parameter family of level curves and select those that stand out to be included in the visualization.

For the lack of a streamfunction in 3-D flows, the above program can only be carried out for streamsurfaces of integrable 3-D flows, such as steady Euler flows that do not satisfy the Beltrami property. For such flows, the Bernoulli function provides a non-degenerate first integral (Arnold & Khesin 1999) whose one-parameter family of level surfaces can be scanned and filtered to obtain the required representative set of streamsurfaces. A similar result is available for incompressible velocity fields with a volume-preserving symmetry group (Haller & Mezić 1998). For general 3-D incompressible flows, however, no first integrals will exist. This is because even steady 3-D flows can be chaotic (see, e.g. Dombre *et al.* 1986) and hence cannot have smooth non-trivial conserved quantities. This is equally valid for the autonomous 3-D differential equation defining the instantaneous streamlines of a generic 3-D unsteady flow, excluding the existence of a regular foliation of the flow domain by streamsurfaces that are level sets of a smooth scalar function.

Often, however, the most important parts of a flow turn out to be vortical regions filled with tubular or toroidal streamsurfaces. One cannot expect these surfaces to necessarily form a continuous family, especially the toroidal ones. Indeed, families of 2-D tori composed of streamlines typically form Cantor sets (as opposed to a continuous family) in the 3-D set of differential equations generating the streamlines (Cheng & Sun 1989). While this is also the case for classic Hamiltonian systems admitting families of invariant tori (Arnold 1989), those systems nevertheless turn out to be integrable restricted to this Cantor set of tori in an appropriate sense (see Chierchia & Gallavotti 1982; Pöschel 1982). Specifically, smooth functions can be constructed that act as first integrals over the Cantor family of tori but not in the small gaps among those tori.

Motivated by this idea of integrability over Cantor sets in Hamiltonian systems, we seek here smooth scalar functions that serve as approximate first integrals over a set of streamsurfaces forming vortical (elliptic) regions of a given vector field. As there is no widely accepted definition of a vortex, we use the term ‘vortical’ loosely to describe families of toroidal or cylindrical surfaces to which either the velocity, vorticity or barrier field is tangent. The approximate first integrals arising from this procedure will be steady for steady vector fields and time-varying for unsteady vector fields. We construct these (approximate) first integrals by seeking scalar functions whose gradient vector field is as close to being normal to the given vector field as possible. To avoid the trivial solution to this problem, we use a constrained minimization approach that does not allow for globally constant first integrals.

Our method resembles that of Yang & Pullin (2010) for the construction of VSFs in inviscid, analytic and highly symmetric flows. Ours, however, differs crucially in that we work with a grid in the physical space over which we expand the unknown approximate first integral in a Fourier series. We then only use the known values of the vector field at the gridpoints. We find that this approach results in an homogeneous linear system of equations whose unique, unit-norm least-squares solution yields the unknown Fourier coefficients of the approximate first integral. Thus, in contrast to Yang & Pullin (2010), this procedure is free from any symmetry assumptions on the first integral and does not require rewriting the homogeneous system as an inhomogeneous one under further assumptions. As we show in one of the appendices, these features of our approach significantly enhance the quality of the final solution.

Outside elliptic regions (i.e. in hyperbolic streamline domains), the streamlines are generically chaotic and hence will admit only trivial approximate first integrals. Accordingly, we expect the approximate first integrals to be nearly constant outside vortical regions, while admitting non-trivial shapes inside such regions. In those elliptic regions, level sets of the approximate first integrals will be close to streamsurfaces that form vortical features.

The result of this approach is an automated numerical visualization method that does not require the user to guess seed points in the flow for streamsurfaces in vortical regions. The simplicity and generality of the proposed method allows us to employ it to complex flows defined either analytically or through numerical data. Our examples include spatially periodic integrable and non-integrable flows, a non-periodic vortex ring flow, a V-junction flow and a fully developed turbulent channel flow. The latter flow exemplifies a case wherein exact streamsurfaces tend to obscure the visualization of the most prominent features of the barrier field. Indeed, for such a flow, vortical regions have been delineated via diagnostic tools such as the active version of the finite-time Lyapunov exponent (aFTLE), as described by Haller *et al.* (2020). Yet, tracking barrier streamlines originating in the neighbourhood of aFTLE ridges quickly results in the streamsurface falling apart, despite some initial vortical motion. In contrast, the structures based on the approximate first integral are able to follow closely the valleys around the aFTLE ridges allowing for a better visualization.

To obtain these results, we divide the computational domain into smaller subdomains and seek approximate first integrals in each one of them separately. In this way, we can capture the most salient structures up to a given scale without the problem of obstruction by smaller structures. These in turn can be captured by further refining the domain subdivision based on their signatures in the aFTLE field. Further, upon assuming mild convexity for the vortical structures to be extracted, we obtain families of barrier surfaces whose outermost members act as vortex boundaries. Thus, we propound a way out of the isocontour value dilemma that besets the typical vortex identification criteria used in the literature (Kim, Moin & Moser 1987; Jeong & Hussain 1995; Zhou *et al.* 1999), causing them to produce dissimilar structures for different isocontour values.

2. Set-up of the minimization scheme and reconstruction algorithm

Let $\boldsymbol{v}(\boldsymbol{x}, t)$ be a smooth vector field defined on some open subset $U \subseteq \mathbb{R}^3$. The associated dynamical system for the instantaneous streamlines of this vector field at time t is given by

$$\boldsymbol{x}' = \boldsymbol{v}(\boldsymbol{x}, t), \quad \boldsymbol{x} \in U, \tag{2.1}$$

where the prime denotes differentiation with respect to a curve-parameter $s \in \mathbb{R}$ along the streamline. A continuously differentiable, scalar function $H(\boldsymbol{x}, t)$ is called an (instantaneous) first integral for $\boldsymbol{v}(\boldsymbol{x}, t)$ at time t if it is constant along each solution of (2.1), i.e. $(\partial/\partial s)H(\boldsymbol{x}(s), t) = 0$. This condition implies that

$$\nabla H(\boldsymbol{x}, t) \boldsymbol{\cdot} \boldsymbol{v}(\boldsymbol{x}, t) = 0, \tag{2.2}$$

for all $\boldsymbol{x} \in U$, where ∇ denotes the gradient with respect to $\boldsymbol{x}$.

For an arbitrary vector field $\boldsymbol{v}$, no first integral will exist, in general, pointwise, i.e. for all $\boldsymbol{x} \in U$. We may, however, relax the constraint (2.2) by seeking a function $H(\boldsymbol{x}, t)$ that minimizes the functional

$$J[H] = \frac{1}{2} \int_U |\nabla H \boldsymbol{\cdot} \boldsymbol{v}|^2 \, \mathrm{d}V, \tag{2.3}$$

which measures the average deviation of $H(\boldsymbol{x}, t)$ from being an exact, pointwise first integral in the domain U at time t. Any minimizer of (2.3) is called an approximate first integral.

First, let us assume that the domain U is triply periodic. This allows us to expand H in a Fourier series and define its modal truncation of order N as

$$H^{\leq N}(\boldsymbol{x}) = \sum_{0<|\boldsymbol{k}|\leq N} \hat{H}_{\boldsymbol{k}} \mathrm{e}^{\mathrm{i}\boldsymbol{k}\boldsymbol{\cdot}\boldsymbol{x}}. \tag{2.4}$$

For the application to the examples in later sections, let us remark that the truncated expansion (2.4) can also be used locally on non-periodic domains, as long as we stay away from the domain boundaries. The integrand of the functional (2.3) in Fourier basis takes the form

$$\nabla H \boldsymbol{\cdot} \boldsymbol{v} = \sum_{0<|\boldsymbol{k}|\leq N} \hat{H}_{\boldsymbol{k}} \mathrm{e}^{\mathrm{i}\boldsymbol{k}\boldsymbol{\cdot}\boldsymbol{x}} \mathrm{i}\boldsymbol{k} \boldsymbol{\cdot} \boldsymbol{v}. \tag{2.5}$$

Because of the linearity of the gradient operator, the expression in (2.5) is linear in the unknown Fourier coefficients.

We assume that the vector field $\boldsymbol{v}$ is known on a discrete, three-dimensional grid of points which we enumerate from 1 through m, where m is the total number of points. Also, to target data-driven applications specifically, we work with the discretized version of (2.3) using the vector of pointwise inner products defined as

$$\begin{bmatrix} \nabla H_1 \boldsymbol{\cdot} \boldsymbol{v}_1 & \nabla H_2 \boldsymbol{\cdot} \boldsymbol{v}_2 & \cdots & \nabla H_m \boldsymbol{\cdot} \boldsymbol{v}_m \end{bmatrix}^{\mathrm{T}} = \boldsymbol{C}\boldsymbol{h}, \tag{2.6}$$

with $\boldsymbol{C} \in \mathbb{C}^{m\times n}$. Here, n is the number of modes used, $C_{ij} = \exp(\mathrm{i}\boldsymbol{k}_j \boldsymbol{\cdot} \boldsymbol{x}_i)\boldsymbol{k}_j \boldsymbol{\cdot} \boldsymbol{v}_i$ is the (i, j) entry of $\boldsymbol{C}$ and $\boldsymbol{h} = \{\hat{H}_{\boldsymbol{k}} | \boldsymbol{k} \in \mathbb{Z}^3,\ 0 < |\boldsymbol{k}| \leq N\}$ is the vector comprising the Fourier coefficients to be determined. Approximating a first integral through the functional (2.3) then amounts to minimizing the squared vector norm $|\boldsymbol{C}\boldsymbol{h}|^2$. To exclude the trivial solution $H \equiv$ const. from our analysis, we add the constraint $|\boldsymbol{h}|^2 = 1$.

Solving this optimization problem is equivalent to finding the eigenvector corresponding to the minimal eigenvalue of the symmetric matrix $\boldsymbol{A} = \boldsymbol{C}^*\boldsymbol{C}$, where $\boldsymbol{C}^*$ denotes the conjugate transpose of $\boldsymbol{C}$ (see Appendix B). Since the eigenvectors of $\boldsymbol{A}$ are the right-singular vectors of $\boldsymbol{C}$, the solution to our algorithm can also be calculated from the singular-value decomposition (SVD) of $\boldsymbol{C}$.

We refrain from expanding the known vector field $\boldsymbol{v}$ into a Fourier series and we write down (2.2) explicitly for every point in the computational grid without working with the coefficients of each Fourier mode. These features distinguish our method from the one presented by Yang & Pullin (2010), as already noted in § 1. This difference will allow us to obtain unique solutions as well as apply our approach even to turbulent flows without additional assumptions.

In the absence of further constraints, the resulting approximate first integral H will, generally, be a complex-valued scalar field. Denoting by H_r and H_i its real and imaginary parts, respectively, we have $\langle \nabla H, \boldsymbol{v}\rangle_{\mathbb{C}} = \langle \nabla H_r, \boldsymbol{v}\rangle - \langle \nabla H_{\mathrm{i}}, \boldsymbol{v}\rangle\, \mathrm{i}$. This implies that by considering the expression in (2.6), we essentially optimize both the real and imaginary parts of H. This allows us to use $|H|$ as the approximate first integral. Alternatively, we can require H to be real *a priori*. We discuss the latter procedure in Appendix C and show that its results are similar to those obtained without imposing this constraint.

As already noted, for generic flows, a non-trivial approximate first integral is only expected to exist in vortical regions. Outside such regions, we expect our algorithm to yield almost flat first integrals. Such a function, locally supported on several vortical regions, would generally require a large number of Fourier basis functions, which in turn would lead to numerical inefficiencies and cost. To avoid this, we work with a comparably small number of basis functions and only use the level surfaces of the emerging approximate first integral in regions where those surfaces are indeed nearly tangent to the given vector field. To identify such regions, we introduce the invariance error as

$$E_A = \frac{1}{A}\sum_{i=1}^{p}\left|\frac{\nabla\,|H_i|\cdot\boldsymbol{v}_i}{|\nabla\,|H_i||\,|\boldsymbol{v}_i|}\right|, \tag{2.7}$$

where A is the surface area of a level set and p the number of points in the level set. This type of error estimate was first introduced by Yang & Pullin (2010). In our visualizations, we will discard streamsurface candidates with invariance errors exceeding a certain threshold value.

Finally, we note that our minimization procedure can also be viewed as finding for $\boldsymbol{v}$, in the appropriate norm, the closest member of the integrable, 3-D incompressible vector field family

$$\boldsymbol{x}' = \boldsymbol{J}(\boldsymbol{x})\nabla H(\boldsymbol{x},t), \quad \nabla\cdot\boldsymbol{J}\equiv\boldsymbol{0}, \tag{2.8}$$

with $\boldsymbol{J} = -\boldsymbol{J}^{\mathrm{T}}$ and $\nabla\cdot\boldsymbol{J}$ denoting the divergence of the tensor field $\boldsymbol{J}$. Indeed, all these vector fields in (2.8) share the same streamsurfaces, the level sets of H. Working with (2.8) directly, however, is much more demanding numerically in our experience and would also require specific assumptions on the form of $\boldsymbol{J}$.

Before moving to specific examples, we note that finding an exact, pointwise first integral in (2.2) is not a well-posed problem by itself. Indeed, if $H(\boldsymbol{x}, t)$ is a solution, then, for any sufficiently smooth function F, $F(H(\boldsymbol{x}, t))$ will also be a solution due to the homogeneity of (2.2). This would not be an issue for the detection of streamsurfaces if the isocontours of H and $F(H)$, expressed through the gradient of these fields, represent the same geometric and topological features for the given vector field $\boldsymbol{v}$. Unfortunately, we can construct simple counter-examples where this is not the case. For instance, if we denote by v_x, v_y and v_z the three components of $\boldsymbol{v}$ and assume that $v_x = 0$, then the function $G(x)H(y,z)$ will be an exact, pointwise first integral as long as $v_y\theta_y H + v_z\theta_z H = 0$. By tweaking G, one can easily obtain markedly different topological features resulting from the corresponding streamlines. We also refer to Pullin & Yang (2014) for more examples of first integrals with different topology for the vorticity field of the Taylor–Green flow stemming from the superposition of independent solutions to (2.2).

Consequently, our variational principle (2.3) will exhibit the same non-uniqueness issues whenever an exact, pointwise first integral is admitted by the underlying vector field. To resolve this, we will only consider approximate first integrals for which the weakest eigenvalue of $\boldsymbol{A} = \boldsymbol{C}^*\boldsymbol{C}$ is not considered (numerically) zero. In addition, we will only retain the streamsurfaces whose topology remains unaltered when, for the same set of grid points, a larger number of Fourier modes is used allowing for small geometric refinements due to the increased accuracy of the solution. If these two conditions are met, we will consider the resulting structures as robust and they will be included in the visualization. Furthermore, we will see that the more complex a flow is, the larger the spectral gap to the second-smallest eigenvalue will be. Irrespective of this gap, however, in all the examples that follow, we will build our solution based only on the eigenvector corresponding to the smallest eigenvalue of $\boldsymbol{A}$. We close this section by noting that our approach is in agreement with the findings of Xiong & Yang (2017, 2019) who showed that the construction of VSFs in turbulent flows through the use of partial differential equations leads to robust structures despite the non-uniqueness issues.

3. Approximate first integrals for explicit solutions of the Euler equations

In this section, we illustrate our minimization algorithm to construct approximate first integrals and use their level sets as approximate streamsurfaces in analytic examples.

3.1. *ABC flow*

As a first test case, we investigate the ABC (Arnold–Beltrami–Childress) class of flows (Dombre *et al.* 1986; Henon 1966), defined as

$$\left.\begin{aligned} \dot{x} &= A\sin z + C\cos y, \\ \dot{y} &= B\sin x + A\cos z, \\ \dot{z} &= C\sin y + B\cos x, \end{aligned}\right\} \tag{3.1}$$

for $A, B, C \in \mathbb{R}$ and $(x, y, z) \in [0, 2\pi]^3$, together with periodic boundary conditions. The right-hand side of (3.1) defines an exact steady solution to the incompressible Euler equations. For $ABC \neq 0$, the flow exhibits chaotic behaviour (Dombre *et al.* 1986; Henon 1966), whereas some analytic non-integrability results have been reported by Ziglin (1988, 1998).

3.1.1. *Integrable case*

We first analyse the ABC flow with $A = 0$ for which (3.1) is completely integrable. For $BC \neq 0$, an exact, pointwise first integral is given by $H_1(x, y) = C\sin y + B\cos x$, while another independent first integral can be constructed through the use of elliptic functions (Llibre & Valls 2012). The level sets of H_1 are depicted in figure 1(*a*) on one cross-section of the computational domain for $B = \sqrt{2}$ and $C = 1$. These curves, therefore, represent the intersections of a representative set of streamsurfaces with the $z = 0$ plane. These streamsurfaces are also exact invariant manifolds for the Lagrangian particle motions in this steady flow.

To test our proposed algorithm for constructing approximate first integrals, we start from a discretized version of the full 3-D velocity field (3.1) along 100 points per direction, using approximately 9000 Fourier modes in (2.4)–(2.6). Solving the underlying optimization problem using the algorithm in Appendix B, we obtain the results shown in figure 1(*b*) at the same cross-section as in figure 1(*a*). The numerically constructed approximate level sets match the analytic first integral closely. To measure the proximity of streamsurfaces and approximate streamsurfaces along the $z = 0$ plane, we introduce a planar version of the general invariance error (2.7) by defining

$$E_l = \frac{1}{l}\sum_{j=1}^{p}\left|\frac{\nabla\left|H_j\right|\cdot\nabla H_{1j}}{\left|\nabla\left|H_j\right|\right|\left|\nabla H_{1j}\right|}\right|, \tag{3.2}$$

where l is the length of the level and p is the number of points for each level set. We use this metric to remove level curves with fewer than 30 points and those with invariance

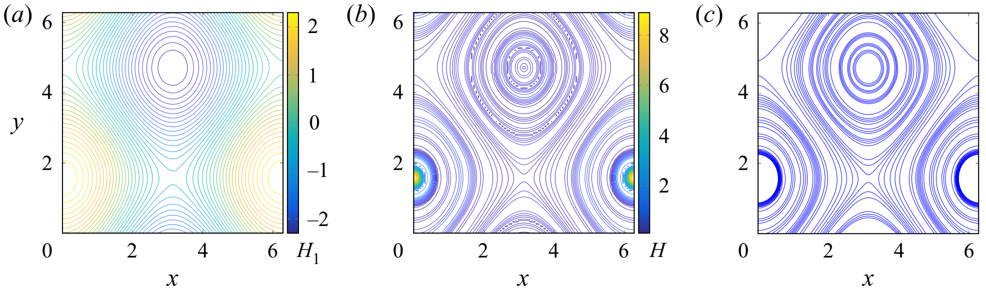

Figure 1. Analysis of the integrable ABC flow using a computational grid of 100^3 points and approximately 9000 Fourier modes. (*a*) Intersections of the level surfaces of H_1 with the $z = 0$ plane. (*b*) Intersections of the level surfaces of the approximate first integral H with the $z = 0$ plane. (*c*) Same as panel (*b*) but after the removal of small-scale structures of panel (*b*) as well as the structures with $E_l > 10^{-5}$.

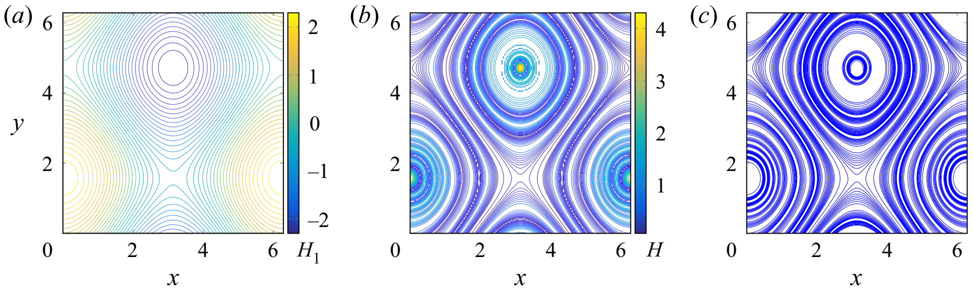

Figure 2. Same as figure 1 but with a computational grid of 150^3 points and 1200 Fourier modes.

errors $E_l > 10^{-5}$. The results shown in figure 1(*c*) confirm that choosing these thresholds removes small-scale artefacts arising from numerical inaccuracies.

We perform the same analysis on the $z = 0$ plane using 150 points per direction but only approximately 1200 Fourier modes. The results are depicted in figure 2. Again, we observe close agreement between the known first integral and the reconstructed curves. At some points, the agreement is even closer when compared to figure 1(*c*) due to the higher spatial resolution, even though the number of Fourier modes is significantly smaller.

3.1.2. *Non-integrable case*

For a different set of parameter values ($A = \sqrt{3}$, $B = \sqrt{2}$ and $C = 1$), the ABC flow (3.1) is non-integrable and shows chaotic behaviour in some regions. The dynamic behaviour of trajectories for this set of parameter values is well studied, including the KAM-type tori highlighted by Poincaré maps (Dombre *et al.* 1986) and elliptic Lagrangian coherent structure (LCS) techniques (Blazevski & Haller 2014; Oettinger, Blazevski & Haller 2016). We use this velocity field as a benchmark to test different solution algorithms for finding an approximate first integral for a non-integrable flow. Also, this will serve as a proof of concept for finding elliptical regions.

We have already noted that the unit-norm least-squares solution to the homogeneous system of (2.6) coincides with the right-singular vector of $\boldsymbol{C}$ associated with its smallest singular value or, equivalently, with the eigenvector associated with the smallest eigenvalue of $\boldsymbol{A} = \boldsymbol{C}^*\boldsymbol{C}$. To improve numerical stability, the SVD-based solution is preferred (Golub & Pereyra 1973). Indeed, the eigenvalue calculation requires a matrix multiplication to form $\boldsymbol{A}$, which invariably squares the condition number of $\boldsymbol{C}$. For comparison, we calculate both the singular-vector-based and the eigenvector-based solutions on the triply periodic box $[0, 2\pi]^3$ with 100 points per direction and $N = 13$ (or 9170 Fourier modes). In this setting, running the SVD algorithm of MATLAB on $\boldsymbol{C}$, which is a $(10^2)^3 \times 9170$ matrix, would require an exorbitant amount of memory (more than 400 GB), indicating that the classical SVD algorithm is not optimized for tall-skinny matrices (such as our coefficient matrix). To proceed with our comparison test, we instead follow the modified SVD method discussed in Appendix D for tall-skinny matrices.

With this modification to the SVD-based solution, the results from the two approaches for the non-integrable ABC flow are presented in figure 3 on the $z = 0$, $y = 0$ and $x = 0$ planes. We observe that the differences between the eigenvector-based and singular-vector-based computations are marginal, indicating that the larger condition number of $\boldsymbol{A}$ does not affect the results. Furthermore, we use the same three planes as Poincaré sections to integrate trajectories up to an arclength of 10^4 from a uniform grid of 20×20 initial conditions on each section. We observe a very good agreement between the predicted structures and the intersections of the KAM surfaces with each of these sections. This is highlighted perhaps even better by the reconstructed KAM surfaces as approximate streamsurfaces in figure 4, which are to be contrasted with the λ_2-based structures in Appendix A. Since the ABC flow is a Beltrami flow, its velocity $\boldsymbol{v}$ is parallel to the vorticity $\boldsymbol{\omega} = \nabla \times \boldsymbol{v}$ (in fact, $\boldsymbol{v} = \boldsymbol{\omega}$); consequently, the approximate-first-integral-based tori we have constructed are also VSFs. This illustrates that our algorithm can identify VSFs in flows where the methodology of Yang & Pullin (2010) is inapplicable. Indeed, as already noted, the non-integrable ABC flow has chaotic streamlines and, thus, no symmetry assumptions regarding these streamlines can be used to accelerate the convergence rate for the optimization technique presented by Yang & Pullin (2010). Even if this rate was irrelevant, however, expanding the known velocity field in a Fourier series would result in an optimization problem with many (numerically) zero eigenvalues and, thus, infinitely many possible minimizers.

Upon taking a closer look at the results of figure 3, we notice that the reconstructed level sets attain their values in a longer range (i.e. [0, 3.5]) for the larger KAM surfaces, whereas, in the vicinity of the smaller structures, they are confined to a narrow band (i.e. [0.25, 0.35]). Here the adjectives larger and smaller are used to refer to either the area (figure 3) or the volume (figure 4) these families enclose. This is a type of overfitting that we would like to mitigate. One way to achieve this is by considering a slightly different optimization problem (see Appendix E) which resembles the one put forward by Yang & Pullin (2010). This different approach, however, turns out to be computationally intense, posing severe limitations on its use for typical grid sizes while its results are arguably of inferior quality. All in all, obtaining the solution to the proposed algorithm as the eigenvector corresponding to the smallest eigenvalue of $\boldsymbol{A}$ is computationally superior to all the other techniques used and, thus, it is the one that we will follow in the rest of this article.

We conclude this section by performing a convergence analysis for different numbers of modes in figure 5. We observe that the least-squares error (as the smallest eigenvalue of $\boldsymbol{A}$) approaches zero as the number of modes used in the analysis increases. Furthermore, the second smallest eigenvalue converges to the smallest one for higher modes. In Appendix B, we show that when the smallest eigenvalues are almost equal, we can construct the solution as a linear combination of the eigenvectors corresponding to these near-identical eigenvalues. Here, however, we can base our solution only on the weakest eigenvector

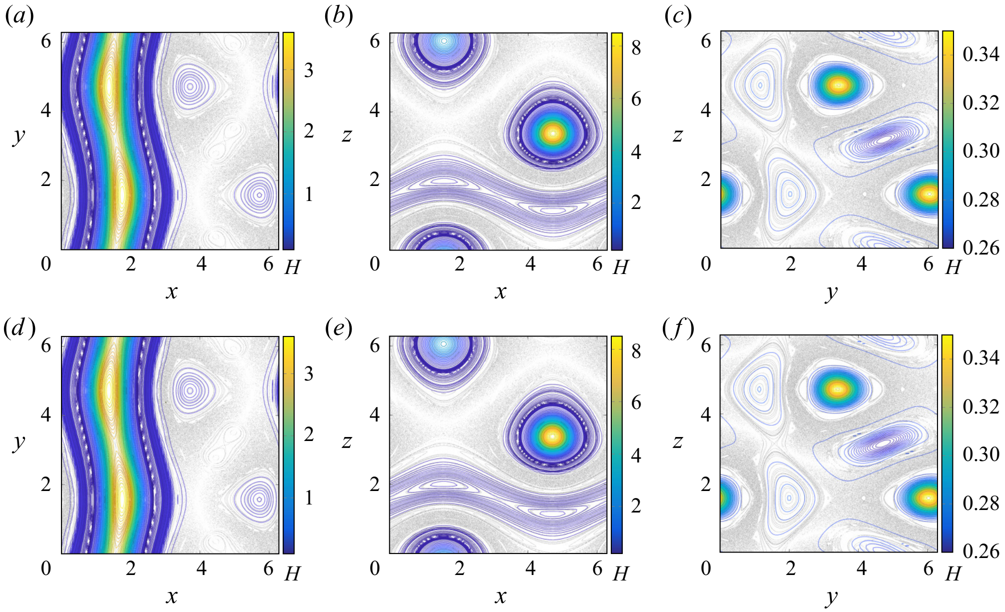

Figure 3. Analysis of the non-integrable ABC flow using a computational grid of 100^3 points and 9170 Fourier modes. Level sets of the approximate first integral at (a,d) $z = 0$, (b,e) $y = 0$ and (c,f) $x = 0$. Panels (a–c) are constructed from the eigenvector of $\boldsymbol{A}$ corresponding to the smallest eigenvalue, whereas panels (d–f) are produced using the SVD of $\boldsymbol{C}$. The overlaid Poincaré map (black dots) on each section is based on a uniform grid of 20×20 initial conditions.

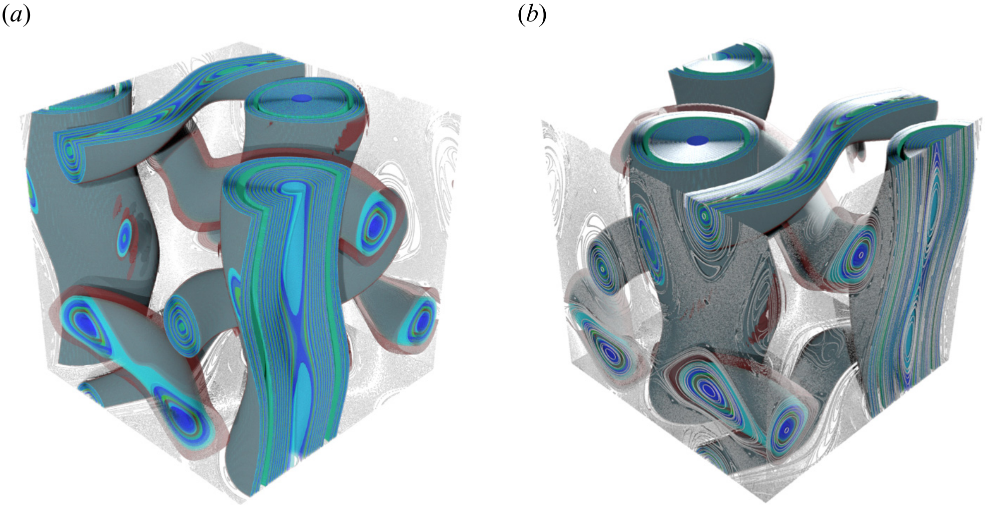

Figure 4. Two different views of the approximate streamsurfaces (level sets of the approximate first integral) closely approximate the KAM-type surfaces of the non-integrable ABC flow in elliptic regions. Also shown are iterations of the Poincaré map (black dots) on three orthogonal planes. The results were obtained using the weakest eigenvector of the positive definite matrix $\boldsymbol{A}$. See also the supplementary movie 1 available at https://doi.org/10.1017/jfm.2022.992.

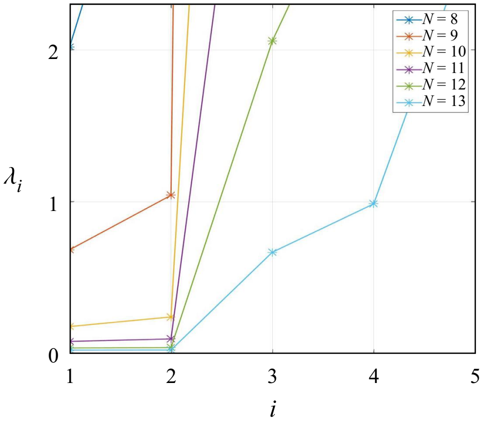

Figure 5. Five smallest eigenvalues of $\boldsymbol{A} = \boldsymbol{C}^*\boldsymbol{C}$ for different numbers of modes (2108, 3070, 4168, 5574, 7152, 9170 modes for $N = 8, 9, 10, 11, 12, 13$, respectively).

since we have $d_1 = 0.015415$ and $d_2 = 0.01596$ for $N = 13$. This gap between d_1 and d_2 will prove significantly larger in the following, data-based examples, confirming the uniqueness of solutions to the optimization problem.

3.2. *Further analytic solution to the Euler equations*

A set of analytic, unsteady, tri-periodic laminar solutions of the Navier–Stokes equations was put forward by Antuono (2020). Here, we consider only the steady part of these solutions, which is a Beltrami solution to the Euler equations with no known first integral. We therefore expect the streamlines of this velocity field to be chaotic and the overall dynamics to be non-integrable. Representative (approximate) streamsurfaces have not yet been constructed for this flow in the literature.

The velocity field is given by

$$\boldsymbol{v} = \frac{4\sqrt{2}}{3\sqrt{3}} \begin{pmatrix} \sin\left(x - \dfrac{5\pi}{6}\right)\cos\left(y - \dfrac{\pi}{6}\right)\sin(z) - \cos\left(z - \dfrac{5\pi}{6}\right)\sin\left(x - \dfrac{\pi}{6}\right)\sin(y) \\ \sin\left(y - \dfrac{5\pi}{6}\right)\cos\left(z - \dfrac{\pi}{6}\right)\sin(x) - \cos\left(x - \dfrac{5\pi}{6}\right)\sin\left(y - \dfrac{\pi}{6}\right)\sin(z) \\ \sin\left(z - \dfrac{5\pi}{6}\right)\cos\left(x - \dfrac{\pi}{6}\right)\sin(y) - \cos\left(y - \dfrac{5\pi}{6}\right)\sin\left(z - \dfrac{\pi}{6}\right)\sin(x) \end{pmatrix}. \tag{3.3}$$

Using a uniform grid of 20×20 initial conditions on the $y = 0$ plane, we integrate trajectories up to an arclength of 10^4 and, upon retaining their long-term behaviour from the interval $[5 \times 10^3, 10^4]$, we show the resulting Poincaré map in figure 6(*a*) where a plethora of KAM tori are discernible. Selecting the triply periodic box $[0, 2\pi]^3$ and sampling it with 100^3 points, we run our algorithm for $N = 13$. Upon constructing isosurfaces for 10 different isovalues of the resulting approximate first integral, we locate their intersections with the $y = 0$ plane and superimpose them on figure 6(*a*). We then compute the invariance error based on (2.7) and colour the isocontours of figure 6(*a*) blue or red depending on whether their average error corresponds to an angle of less or more than 5°. Based on this, contours lying inside the chaotic sea of the Poincaré map show the

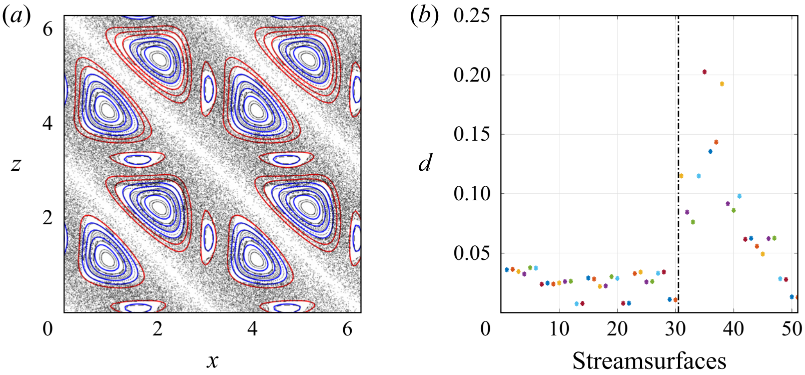

Figure 6. (*a*) Comparison of the Poincaré map on the plane $y = 0$ for the steady Euler flow (3.3) overlaid on the intersections of the tori obtained from an approximate first integral with the same plane for $N = 13$. The blue (red) isocontours depict tori whose invariance error (see (2.7)) is smaller (larger) than 5° on average. (*b*) 95th percentile of the distance (in non-dimensional units) between trajectories emanating from the isocontours of panel (*a*) with the corresponding 2-D tori inside the computational box $[0, 2\pi]^3$. The points to the left (right) of the dash–dotted line correspond to trajectories originating in the blue (red) contours of panel (*a*).

largest invariance error despite our algorithm not using any knowledge of the long-term, chaotic dynamics.

For every isocontour of figure 6(*a*), we launch trajectories following the vector field $\boldsymbol{v}$ of (3.3) until they leave the computational domain $[0, 2\pi]^3$, and then calculate their distances from the corresponding isosurfaces. Thus, in figure 6(*b*), we present the 95th percentile of those distances for each streamsurface after separating them according to figure 6(*a*), i.e. we depict the trajectories corresponding to the blue contours in the left side of the dash–dotted line, whereas the ones for the red contours in the right side. We note the correlation between the retained (blue) isocontours of figure 6(*a*) and the significantly smaller percentiles of figure 6(*b*).

Similarly, we present the reconstructed tori for $N = 15$ or 14 146 modes in figure 7(*a*). We observe that for $N = 13$, the approximate first integral captures virtually all the KAM surfaces indicated by the Poincaré map. In contrast, for $N = 15$, some of the structures are captured more accurately while others are missed completely. The convergence analysis depicted in figure 8(*a*) shows that the least-squares error follows a declining trend as N grows. This prompts us to consider an error measure similar to the one in (2.7), defined as

$$E_m = \frac{1}{m} \sum_{i=1}^{m} \left| \frac{\nabla\, |H_i| \cdot \boldsymbol{v}_i}{|\nabla\, |H_i||\, |\boldsymbol{v}_i|} \right| . \tag{3.4}$$

In this expression, the summation is taken over all the grid points, providing an estimate for the mean invariance error of the entire solution. This allows us to make a direct comparison among solutions corresponding to different numbers of modes. Specifically, excluding points that lie in the vicinity of fixed points of either $\boldsymbol{v}$ or $\nabla|H|$, we show the dependence of the invariance error E_m on the number of Fourier modes used in our algorithm in figure 8(*b*). We observe that the error attains the minimum value for $N = 13$, in agreement with what is inferred from figure 6(*a*).

Moreover, to mitigate minor discrepancies between the reconstructed tori and those outlined by the Poincaré map of figure 6(*a*), we increase the number of Fourier modes to 28 670 ($N = 19$), while keeping the same set of grid points. A closeup view of a region

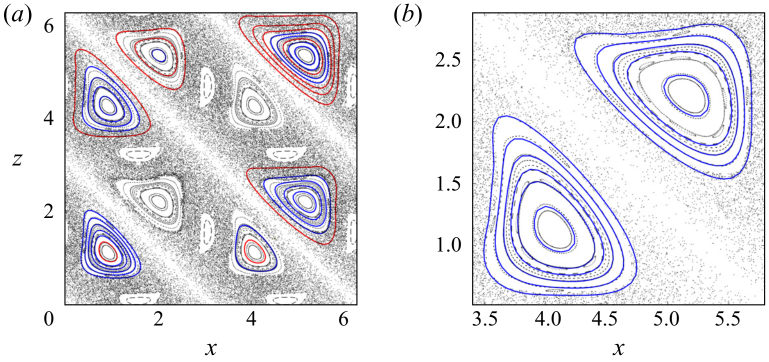

Figure 7. (*a*) Same as in figure 6(*a*) with the tori reconstructed for $N = 15$. (*b*) Closeup view on a region filled with two families of invariant tori. Overlaid on the Poincaré map are the tori obtained from an approximate first integral for $N = 19$.

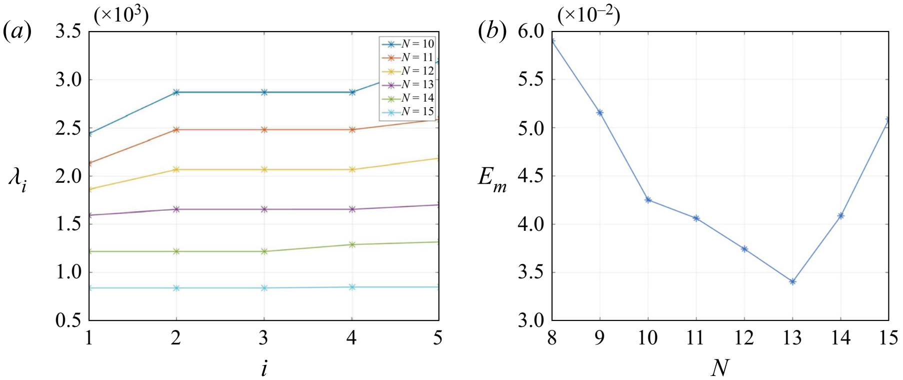

Figure 8. Numerical details of the approximate first integral calculation for the steady Euler flow (3.3). (*a*) Five smallest eigenvalues of $\boldsymbol{A} = \boldsymbol{C}^*\boldsymbol{C}$ and (*b*) normalized error estimate (3.4) for different numbers of modes.

filled with invariant tori in figure 7(*b*) confirms that there is a close agreement with the tori obtained from an approximate first integral. There is, however, a trade-off between the increased accuracy and the ensuing computational burden that an end user must consider.

We also note that, while for $N = 15$ we have $d_1 \approx d_2 = 839.8079$, for $N = 19$ we have $d_1 = 204.5165$ and $d_2 = 218.2078$, further corroborating that our approach leads to a unique solution. Finally, we conclude this section with figure 9(*a*) showing 3-D rendered images of the three Poincaré maps on the planes $x = y = z = 0$, figure 9(*b*) showing representative streamsurfaces obtained as level surfaces of an approximate first integral for $N = 13$ and figure 9(*c*) showing the superimposition of panel (*a*) on panel (*b*), which confirms the close agreement between the expected and reconstructed structures.

3.3. *Hill's spherical vortex*

We now turn to a spatially non-periodic, integrable flow given by Hill's spherical vortex (Hill 1894). The axial-symmetric (approximately the *z*-axis) streamfunction for Hill's

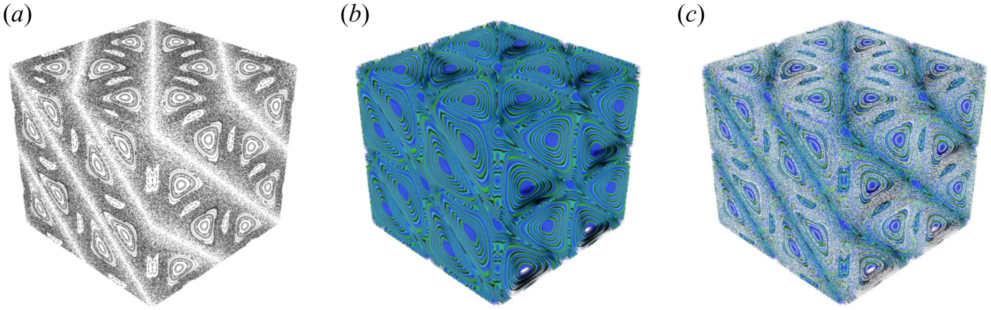

Figure 9. Results for the steady Euler flow (3.3). (*a*) Poincaré maps on $x = y = z = 0$. (*b*) Streamsurfaces approximating the KAM surfaces of (3.3). (*c*) Panel (*a*) superimposed on panel (*b*).

solution to the Euler equations is

$$\psi(h,z) = \begin{cases} \dfrac{3}{4}U_0 h^2\left(1-r^2\right), & r \le 1, \\ -\dfrac{1}{2}U_0 h^2\left(1-\dfrac{1}{r^3}\right), & r > 1, \end{cases} \tag{3.5}$$

where h is the distance from the axis of symmetry ($h^2 = x^2 + y^2$) and $r^2 = h^2 + z^2$. Using the relations $u_h = -(1/h)(\partial\psi/\partial z)$ and $u_z = (1/h)(\partial\psi/\partial h)$, we obtain the corresponding velocity field in Cartesian coordinates

$$\boldsymbol{v}(x,y,z) = \begin{cases} \dfrac{3}{2}U_0\left(xz,\ yz,\ 1-(r^2+h^2)\right), & r \le 1, \\ \dfrac{3}{2}U_0\left(\dfrac{xz}{r^5},\ \dfrac{yz}{r^5},\ \dfrac{2}{3}\dfrac{1}{r^3}-\dfrac{h^2}{r^5}\right), & r > 1. \end{cases} \tag{3.6}$$

As for periodic domains, we can compute a Fourier expansion on a bounded subdomain, bearing in mind that the convergence of the partial Fourier sum will be slow in general (Gottlieb & Shu 1997). To mitigate this issue, we will have to consider a sufficiently high number of modes. Furthermore, due to the well-known Gibbs phenomenon, there will be sizeable spurious oscillations in the approximate first integral near the box boundary that do not diminish after an increase in the number of modes. To damp this effect in our algorithm, we discard all the reconstructed surfaces that fall within 5 % of the box size in all three directions.

The velocity field of (3.6) has toroidal streamsurfaces inside the spherical domain $\{\boldsymbol{x} \in \mathbb{R} : |\boldsymbol{x}| \le 1\}$ (see figure 10*a*). We reconstruct these streamsurfaces over the computational domain $[-2, 2]^3$ with 60 points per direction, running our algorithm for different numbers of Fourier modes with $U_0 = 1$. In some cases with $N < 15$, the non-periodic nature of the velocity field results in the breakdown of the reconstructed toroidal structures. For $N \ge 15$, however, we obtain fully symmetric solutions. Specifically, for illustration purposes, we work with $N = 17$ (or 20 478 Fourier modes) which yields a unique solution corresponding to the smallest eigenvalue of $\boldsymbol{A}$, $d_1 = 23.5169$ ($d_2 = 25.3118$). Based on this, we create 10 isosurfaces in the interval $\left[|H|_{min}, |H|_{max}\right]$. Upon locating the intersections of these surfaces with eight radially equidistant planes, we launch trajectories corresponding to these intersections and compute the pointwise distance of the solution curves to the reconstructed surfaces. The results (in terms of percentiles) are presented in figure 10(*b*). A comparison between the reconstructed streamsurfaces and indicative solution curves is given in figure 11.

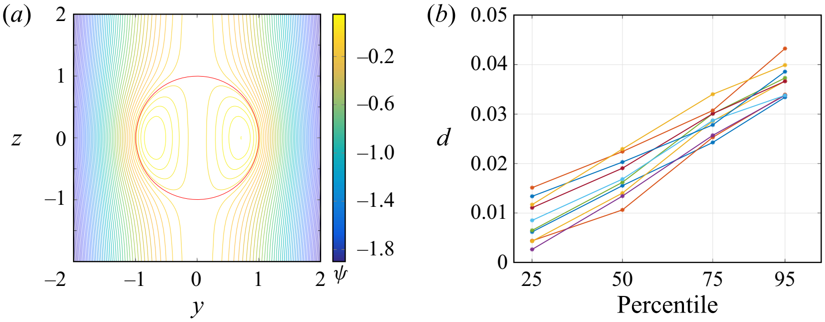

Figure 10. (*a*) Level sets of Hill's streamfunction on the $x = 0$ plane. (*b*) 25th, 50th, 75th and 95th percentile of the pointwise distances (in non-dimensional units) between solution curves and 10 different reconstructed streamsurfaces for $N = 17$.

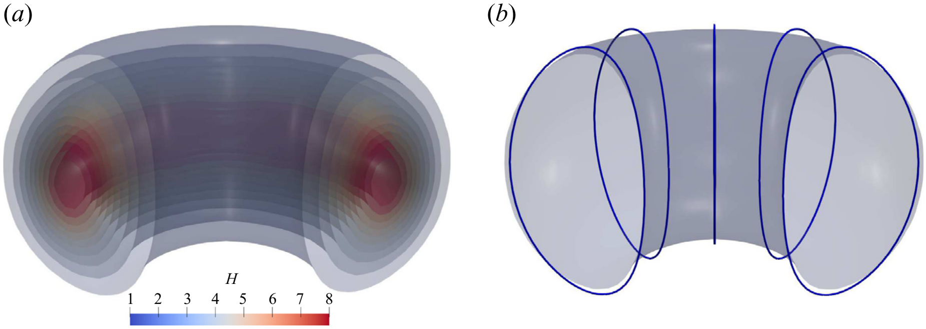

Figure 11. (*a*) Streamsurfaces of figure 10 that have a 95th percentile less than 0.05 for $x > 0$. (*b*) Solution curves of (3.6) for 5 different points lying on the outer streamsurface of panel (*a*).

3.4. *Flow inside a V-junction*

Next we investigate the flow inside a V-junction, as depicted in figure 12. Despite the simple geometry, recent experiments have suggested that pumping a particle-laden fluid into such a configuration allows light particles, such as gas bubbles in water, to be permanently trapped in the junction (Vigolo, Radl & Stone 2014). This phenomenon arises for a wide range of Reynolds numbers and for various junction angles (Ault *et al.* 2016). Here we consider one such flow with junction angle 70° and $Re = (\bar{u}L/\nu) = 230$ (Shin, Ault & Stone 2015), where $\bar{u}$ is the average inlet flow speed, L is the side length of the square channel and ν is the kinematic viscosity.

We use a finite-volume solver from the OpenFOAM library to obtain a steady solution to the 3-D incompressible Navier–Stokes equation (Weller *et al.* 1998). The same numerical solution has recently been analysed using methods from dynamical systems theory, which revealed large, anchor-shaped trapping regions for light particles (Oettinger *et al.* 2018). These trapping regions, however, have been invariably linked to bubble-type vortex breakdown structures in the fluid flow, which are formed downstream in the junction (Ault *et al.* 2016). These structures are depicted as dark grey blobs in figure 12, obtained from a careful advection of streamlines from the vicinity of known stagnation points. Their construction, therefore, is by no means automated and assumes a detailed knowledge of the streamline geometry.

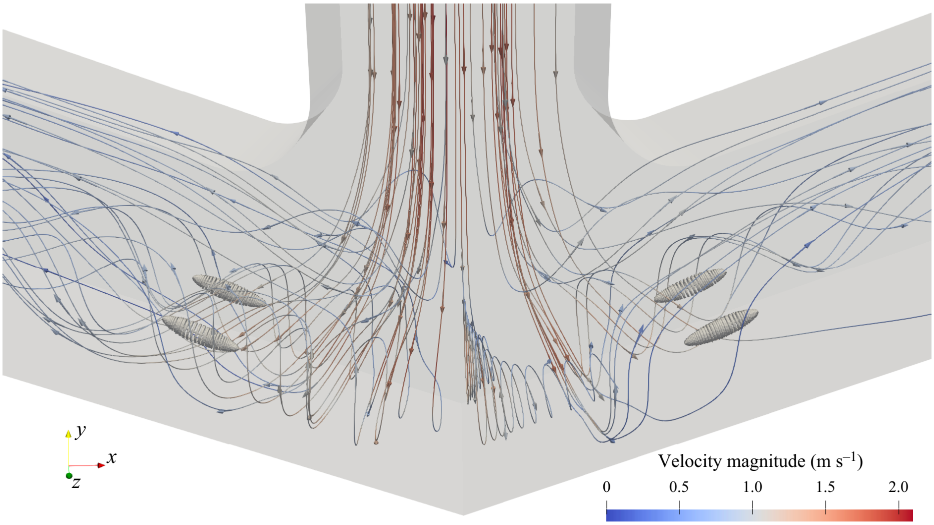

Figure 12. Velocity streamlines, colour coded with their magnitude, emanating from the inlet of the V-junction and leaving the domain from the two outlets. For $Re = 230$ and a junction angle of 70°, four symmetric vortex-breakdown bubbles are portrayed in grey.

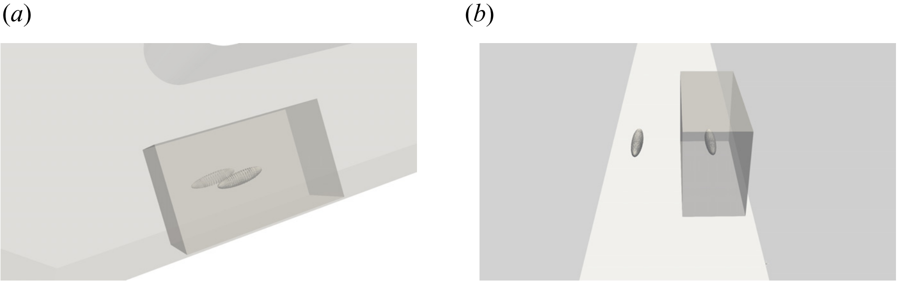

Figure 13. Different views of the computational box used to construct an approximate first integral for one of the bubble-like structures in the V-junction flow.

Each vortex breakdown bubble is demarcated by the 2-D stable and unstable manifolds of two saddle-type fixed points. In a generic 3-D flow, these two manifolds do not coincide because that configuration would not be structurally stable. Instead, they are expected to intersect transversely. In such a scenario, the original streamsurface breaks down allowing fluid particles from the main stream to be entrained into the bubble and, conversely, particles to return from the bubble to the main stream (Holmes 1984; Peikert & Sadlo 2007). Sotiropoulos, Ventikos & Lackey (2001) showed that a very careful mesh refinement is required to reveal the splitting of the manifolds. Here, we will only be interested in reconstructing a closed streamsurface that manifests minimal fluid exchange (see Peikert & Sadlo (2007) for a discussion of this surface).

We select as computational domain the box depicted in figure 13 with 110, 90, 80 points in the x, y and z direction, respectively. This box is chosen so that the bubble-like vortical structure lies approximately in its centre. The dimensions of the box are $L_x = 1$ m, $L_y = 0.6$ m and $L_z = 0.4$ m. This procedure incorporates *a priori* information approximating the rough location of the streamsurface of interest. We will see in the next section how the same algorithm can be extended to uncover *a priori* unknown structures in a turbulent flow.

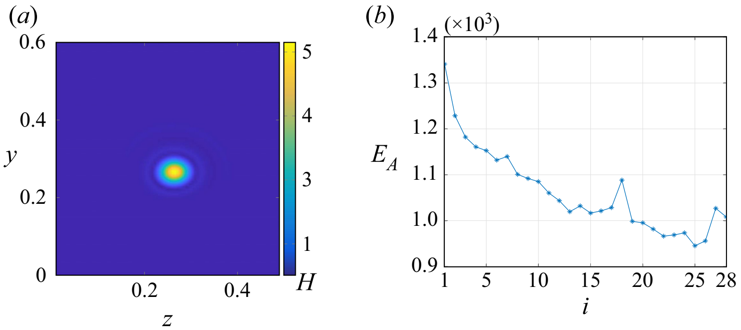

Figure 14. Results for an approximate first integral in the V-junction flow, framing one of the elliptical vortex regions. (*a*) Approximate first integral distribution on a plane which coincides with the middle, in the x direction, of the computational domain presented in figure 13. (*b*) Normalized invariance error as a function of the extracted isosurfaces sorted in descending order with respect to their volume.

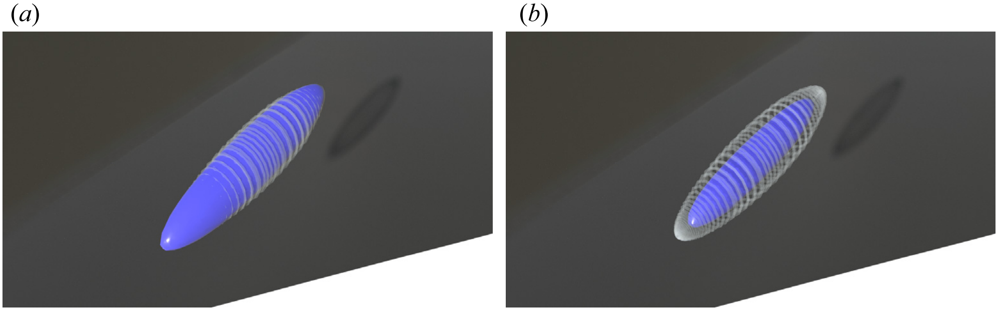

Figure 15. Streamsurfaces as level sets of an approximate first integral in the V-junction flow, corresponding to one local ($i = 15$) and the global minimum ($i = 25$) of the normalized error E_A depicted in figure 14(*b*). The duct is cut transversely to help the visualization.

We use our algorithm with $N = 15$ or 14 146 Fourier modes and show a 2-D cross-section at the middle of the computational domain in figure 14(*a*). For the smallest eigenvalue of $\boldsymbol{A}$, $d_1 = 58.1538$ ($d_2 = 376.9696$), a very pronounced circular structure is clearly visible approximately in the middle of the domain bordering an otherwise flat landscape. To obtain the full, 3-D reconstruction, we use 40 equidistant values between $|H|_{min}$ and $|H|_{max}$ and extract 28 different level surfaces of the approximate first integral. We then sort them in decreasing order based on the volume they enclose.

Plotting this error estimate for the extracted isosurfaces (figure 14*b*) yields a global minimum for the surface $i = 25$ and a local minimum for the surface $i = 15$. Rendered depictions of the extracted isosurfaces corresponding to these two minima are shown in figure 15. We note the close agreement between the reconstructed structures and the structure delineated by the judiciously chosen streamlines. This is in stark contrast to the structures suggested by the Q-criterion as demonstrated in Appendix A.

4. Momentum transport barriers in a turbulent channel flow

As we have mentioned in § 1, the shape of streamsurfaces is observer-dependent: their geometry changes under general time-dependent rotations and translations of the observer. Therefore, unless the flow has a distinguished frame in which streamsurfaces coincide with material surfaces, streamsurfaces simply highlight features of the velocity field in a given frame, as opposed to intrinsic, observer-indifferent features of the flow of fluid particles.

For studies seeking to be consistent with observed flow physics, the latter features are relevant (Haller 2021). This is because flow visualization experiments with dye particles highlight material (and hence objectively defined) transport barriers, which generally differ substantially from streamsurfaces in unsteady flows. At the same time, classic studies focused on momentum, energy or vorticity transport are inherently frame-dependent by the frame-dependence of all these Eulerian fields.

To reconcile these two objectives, Haller *et al.* (2020) developed a theory of objectively defined barriers to the transport of active vector fields, such as the vorticity and momentum. Aksamit & Haller (2022) used this theory to locate instantaneous (Eulerian) frame-indifferent momentum transport barriers in 3-D turbulent channel flows. Active barriers turn out to be distinguished streamsurfaces of appropriately defined steady, 3-D incompressible vector fields (Haller *et al.* 2020). Specifically, momentum transport barriers of a Navier–Stokes velocity field $\boldsymbol{v}(\boldsymbol{x}, t)$ at time t are streamsurfaces of the barrier equation

$$\boldsymbol{x}'(s) = \boldsymbol{\Delta v}\left(\boldsymbol{x}(s), t\right), \tag{4.1}$$

with $s \in \mathbb{R}$ denoting a parametrization of streamlines forming the streamsurfaces and $\boldsymbol{\Delta}$ the Laplace operator. For an incompressible velocity field, we further note that $\boldsymbol{\Delta v} = -\boldsymbol{\nabla} \times \boldsymbol{\omega}$ holds.

Haller *et al.* (2020) and Aksamit & Haller (2022) detected distinguished streamsurfaces of the momentum barrier equation (4.1) using active versions of some of the passive hyperbolic and elliptic LCS diagnostics reviewed by Haller (2015). These Lagrangian calculations involve arrays of trajectories and return diagnostic scalar fields for visual inspection rather than explicit streamsurfaces families. In the following, we will use our approach for finding approximate first integrals to obtain vortical momentum barriers as level surfaces of an approximate first integral for (4.1).

4.1. *Numerical dataset*

We study the 3-D incompressible, turbulent channel flow which can be found here. The friction Reynolds number is $Re_\tau = u_\tau h/\nu = 150$, where u_τ is the friction velocity, h is the channel half-height and ν is the kinematic viscosity. We denote by x, z and y the streamwise, spanwise and wall-normal directions, respectively. The computational domain is $L_x = 2.5\pi h$ long and $L_z = \pi h$ wide.

The number of Fourier modes used in the simulation was 192 in both the streamwise and the spanwise direction. The number of points in the wall-normal direction is 194, inhomogeneously spaced so that the grid becomes more refined closer to the walls. No-slip boundary conditions were applied at the two channel walls and the governing equations were integrated forward in time with a constant pressure gradient $\mathrm{d}p/\mathrm{d}x = -1$ enforced so as to drive the flow through the channel. Ten thousand velocity field snapshots were stored at multiples of the simulation time step $\Delta t = 0.001$ once the flow reached a statistically stationary state. We will identify the 5000th snapshot of this time series with the time $t = 0$.

4.2. *Momentum barrier extraction*

We seek to uncover objectively defined instantaneous momentum transport barriers corresponding to the time $t = 0$ as specific streamsurfaces of the vector field $\boldsymbol{\Delta v}(\boldsymbol{x}, 0)$ in (4.1). First, as illustration of prior results by Haller *et al.* (2020) on this problem, we show the FTLE field computed for $\boldsymbol{\Delta v}(\boldsymbol{x}, 0)$ (called active FTLE or aFTLE) from a

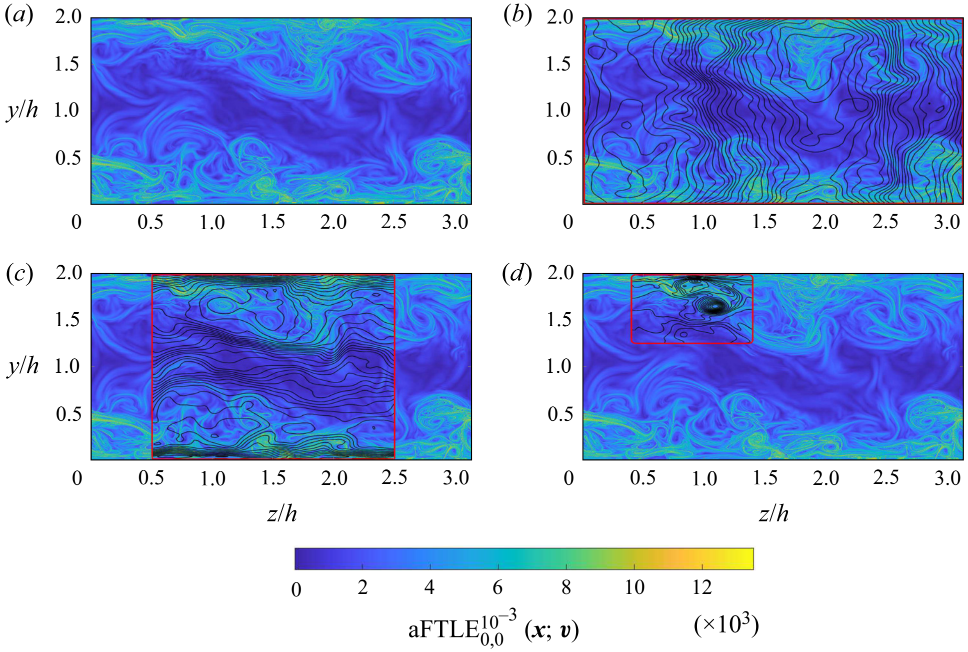

Figure 16. (*a*) Active FTLE (aFTLE) for the momentum barrier field (4.1) at $t = 0$ over a 2-D cross-section of the channel at $x/h = 2$. (*b–d*) Projections of the approximate first integral (black lines) on the same cross-section using as computational domains for the analysis the (red) boxes $[1, 3] \times [0, 2] \times [0, \pi]$, $[1, 3] \times [0, 2] \times [0.5, 2.5]$ and $[1, 3] \times [1.25, 2] \times [0.4, 1.4]$, respectively, superimposed on the aFTLE landscape.

grid of 800×1000 initial conditions uniformly placed in the wall-normal and spanwise directions, respectively, up to $s = 10^{-3}$ (see figure 16*a*). This plot indicates the signatures of two larger barriers to momentum transport, with the first located approximately around $[z/h, y/h] = [0.75, 1.25] \times [1.5, 1.75]$. The second, a mushroom-type barrier, is located around $[2.25, 2.75] \times [1.25, 1.75]$. A plethora of other smaller-scale structures are also present in the aFTLE plots.

We use three different computational domains to illustrate the potential of the algorithm presented in § 2: the boxes $[1, 3] \times [0, 2] \times [0, \pi]$, $[1, 3] \times [0, 2] \times [0.5, 2.5]$ and $[1, 3] \times [1.25, 2] \times [0.4, 1.4]$ with $80 \times 85 \times 80$ points in the streamwise, wall-normal and spanwise direction, respectively. In each of these boxes, the points are evenly spaced and a tri-linear interpolation scheme is employed to obtain the necessary $\boldsymbol{\Delta v}$ values. Moreover, we perform another rescaling of the dummy time s to pointwise normalize the right-hand side of (4.1). This eliminates the high norms of $\boldsymbol{\Delta v}$ near the wall in the expression (2.6). If this normalization is not used, our algorithm tends to miss the turbulent regions close to the wall and touches more on the central part of the channel.

For $N = 13$ (9170 Fourier modes), 20 isovalues of the approximate first integral are depicted in figure 16(*b–d*) on the $x/h = 2$ plane. We note the progressive improvement in the reconstruction of the first structure discussed above, as the computational domain starts to close in on it. This observation prompts us to use a greedy algorithm compartmentalizing the domain into smaller, overlapping domains. The size of these domains will be dictated by the scale of the structures to be extracted.

Our algorithm so far generates families of streamsurfaces. We now seek to locate outermost members of nested elliptical barrier families. To this end, for each of the overlapping computational boxes, we use n_{iso} different values to produce isosurfaces in the interval $[|H|_{min}, |H|_{max}]$. We then group the resulting isosurfaces into foliations (see figure 20(f) for two such foliations) or, more generally, families by finding the ones that either lie entirely inside others or have an intersection volume above a certain threshold, respectively. Subsequently, we discard the foliations or families that have a number of members less than a fixed percentage of n_{iso}. We note that for the isosurface extraction, we use MATLAB's built-in function which is based on the 'Marching cubes' algorithm (Lorensen & Cline 1987). Other techniques generating isosurfaces (see, e.g. the concept of contour trees (Carr, Snoeyink & Axen 2003)) are known to produce robust structures in a more efficient fashion and could certainly be used as viable alternatives.

We also follow Haller *et al.* (2016) and define the convexity deficiency of a closed surface as the ratio of the volume between the surface and its convex hull to the volume enclosed by the surface. Here, however, we will only discard the most non-convex surfaces.

We summarize the main steps of the computations we described previously in Algorithm 1. In the next section, we will use this algorithm to uncover momentum transport barriers tied to different scales in the turbulent channel flow.

Algorithm 1 Extraction of instantaneous barriers to momentum transport

Input: A snapshot of the $\boldsymbol{\Delta v}$ field defined over a 3-D Cartesian grid. Lengths L_x, L_y and L_z as well as number of points N_x, N_y and N_z. Different parameters n_{iso}, p_b, d_{max} and p_f.

```
(i)   Partition the original grid into smaller, overlapping rectangular domains with
      dimension $L_x \times L_y \times L_z$.
(ii)  Use tri-linear interpolation to obtain the values of $\boldsymbol{\Delta v}/|\boldsymbol{\Delta v}|$ on a grid of $N_x \times N_y \times$
      $N_z$ points inside every domain.
(iii) Form the coefficient matrix $\boldsymbol{C}$ and obtain the eigenvector of $\boldsymbol{A}$ corresponding to its
      smallest eigenvalue.
(iv)  Obtain a 3-D scalar field $|H|$ serving as an approximate first integral inside each
      domain and construct $n_{iso}$ isosurfaces out of it.
(v)   Discard the surfaces that have at least one point within $p_b$ percent of either $L_x$, $L_y$ or
      $L_z$ of each domain's face boundaries, respectively. Also, discard all the surfaces that
      have a convexity deficiency ratio larger than a threshold $d_{max}$.
(vi)  Classify the remaining structures into foliations or families after locating the ones
      that either lie entirely inside others or have an intersection volume above a certain
      threshold, respectively. Keep only the foliations or families with more than $p_f \cdot n_{iso}$
      members.
(vii) Plot the member of each foliation or family with the largest volume.
```

Output: Almost convex, frame-indifferent 2-D vortical barriers to momentum transport in the velocity field $\boldsymbol{v}$.

4.3. *Results*

4.3.1. *Channel partition into large subdomains*

To illustrate our algorithm, we use the entire computational domain of the direct numerical simulation (DNS) described in § 4.1. First we partition it in the following overlapping subdomains $[x_{1_i}, x_{2_i}] \times [y_{1_j}, y_{2_j}] \times [z_{1_k}, z_{2_k}]$ with $x_1 \in \{-0.5, 0.5, \ldots, 5.5\}$, $x_2 \in \{1.5, 2.5, \ldots, 7.5\}$, $y_1 \in \{0, 0.5, 1\}$, $y_2 \in \{1, 1.5, 2\}$, $z_1 \in \{0, 1, 2\}$, $z_2 \in \{1.5, 2.5, 3.5\}$, $i = 1, \ldots, 7$, $j = 1, 2, 3$, $k = 1, 2, 3$. For each of these

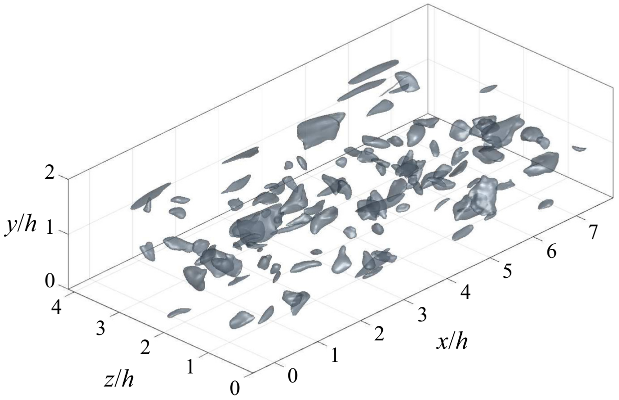

Figure 17. Instantaneous barriers to momentum transport in the 3-D turbulent channel flow, derived using the larger partition described in § 4.3.1.

domains, we use a grid of $70 \times 75 \times 70$ evenly spaced points on which we compute the normalized velocity Laplacian. For the approximate first integral, we use $N = 13$ (or 9170 Fourier modes). This comes as a necessary trade-off between computational time and surface accuracy after we observed that the reconstructed structures do not vary significantly when we use $N = 12$ or $N = 14$. With it, we extract $n_{iso} = 40$ isosurfaces in every domain. Of them, we discard the surfaces described in steps 5 and 6 of Algorithm 1 by employing $p_b = 2\,\%$, $p_f = 10\,\%$ and $d_{max} = 20\,\%$.

The results of this computation are shown in figure 17. We observe that the entire channel is populated by a host of different momentum transport barriers, the majority of which have a clear quasi-streamwise direction. These structures are reminiscent of those investigated in studies of wall-bounded flows (Robinson 1991). The structures we obtain, however, are more evenly scattered throughout the channel, appearing not only near the channel walls but also in the more quiescent central part. This is in stark contrast to typical predictions from classic vortex criteria for these flows (Hunt, Wray & Moin 1988; Chong, Perry & Cantwell 1990; Jeong & Hussain 1995). This phenomenon, i.e. structures penetrating into and spanning the bulk flow region, has already been noted in the literature (Haller *et al.* 2020; Aksamit & Haller 2022) by analysing the 2-D signatures of these structures via diagnostic fields. Here, however, we explicitly construct these structures via the streamsurfaces surrounding them.

4.3.2. *Channel partition into small subdomains*

We now employ smaller partitions of the channel, using the overlapping subdomains $[x_{1_i}, x_{2_i}] \times [y_{1_j}, y_{2_j}] \times [z_{1_k}, z_{2_k}]$ with $x_1 \in \{-0.5, 0, \ldots, 6.5\}$, $x_2 \in \{0.5, 1, \ldots, 7.5\}$, $y_1 \in \{0, 0.5, 1\}$, $y_2 \in \{1, 1.5, 2\}$, $z_1 \in \{0, 1, 2\}$, $z_2 \in \{1.5, 2.5, 3.5\}$, $i = 1, \ldots, 15$, $j = 1, 2, 3$, $k = 1, 2, 3$, while keeping all the other parameters the same as in § 4.3.1.

The results for this computation are shown in figure 18. In this case, we again observe momentum transport barriers that tend to align with the streamwise direction but in larger numbers, when compared with figure 17. Another notable difference is that the reconstructed structures show generally smaller scales than before. This demonstrates that our domain partition algorithm acts as a filter of various scales. This provides a natural way out of the occlusion quandary that besets many visualization approaches while retaining the algorithm's capacity to capture the smallest structures, delineated in

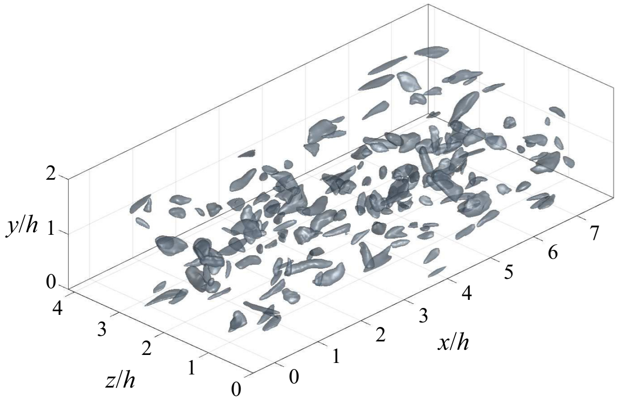

Figure 18. Instantaneous barriers to momentum transport in the 3-D turbulent channel flow, derived using the smaller partition described in § 4.3.2. The supplementary movie 2 of the supplementary material portrays the extracted structures for the time interval $[t_0, t_1] = [0, 0.5]$.

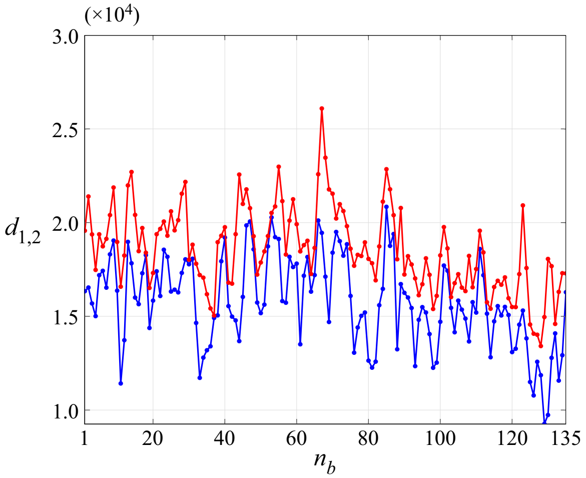

Figure 19. Distribution of the smallest (blue) and the second smallest (red) eigenvalues of $\boldsymbol{A}$ over the different computational domains used for the barriers surfaces presented in figure 18.

the aFTLE plots, by using finer partitions. In the next subsection, we will demonstrate this capacity by pinpointing structures that the active diagnostics-based methods in Haller *et al.* (2020) and Aksamit & Haller (2022) would likely miss. We conclude this section with figure 19 depicting a well-formed spectral gap between the smallest and the second smallest eigenvalue of $\boldsymbol{A}$ for all the computational boxes. Finally, we carry out an unsteady barrier analysis for times varying over the interval $[t_0, t_1] = [0, 0.5]$, as presented in the supplementary movie 2. In it, the fact that some barrier surfaces seem to appear, then disappear and perhaps reappear at a later time is a direct consequence of the flat convexity deficiency threshold we allow for these surfaces (20 %) throughout the channel. We expect this phenomenon to be resolved when the purely Lagrangian approach of Haller *et al.* (2020) is combined with our algorithm in follow-up work.

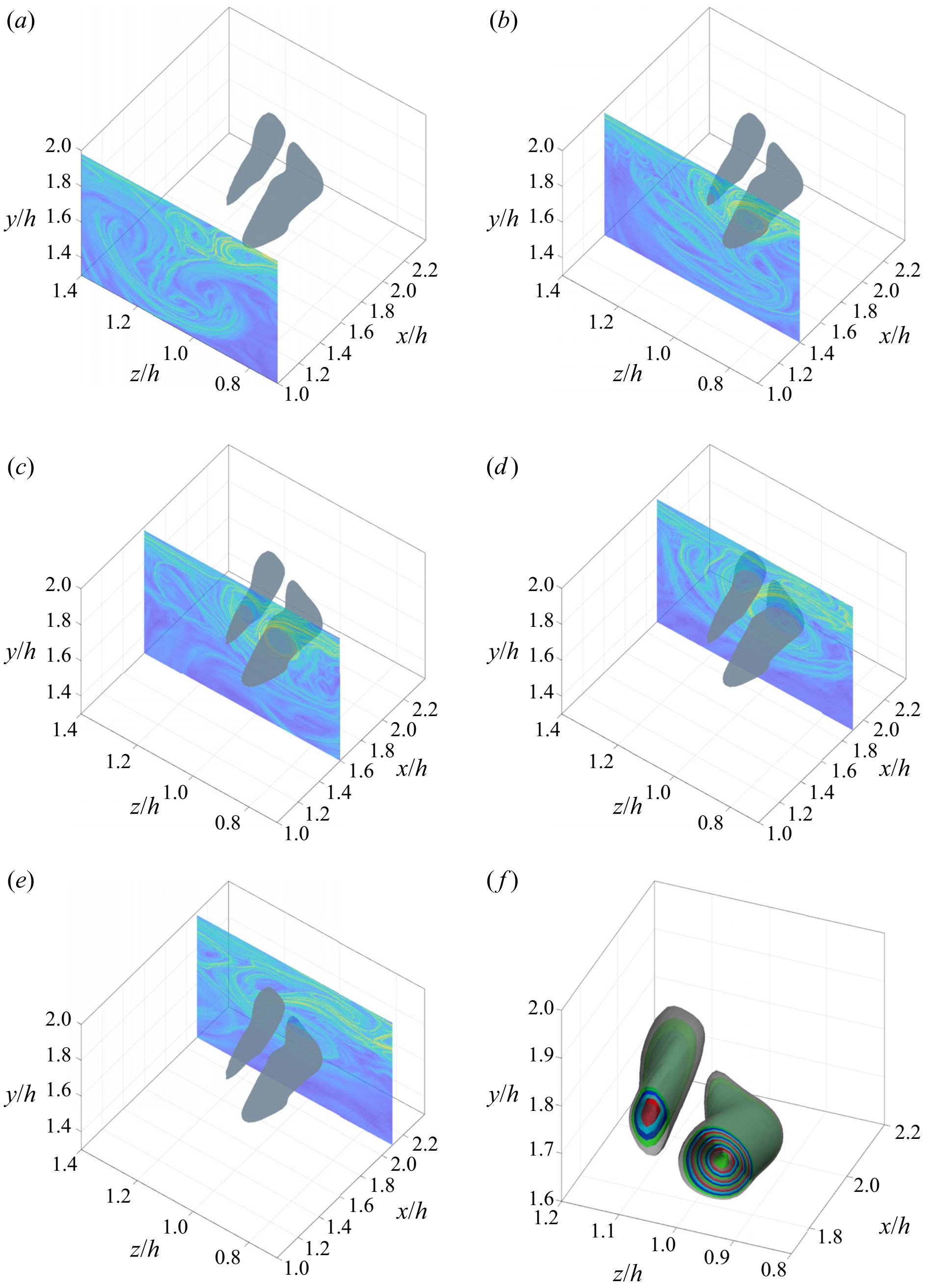

Figure 20. Two branches of a mushroom-like, objective vortex (in grey) captured by Algorithm 1 in the 3-D turbulent channel flow. The branches are superimposed on 2-D cross-sections of the aFTLE field at $x/h = 1$, 1.4, 1.6, 1.9 and 2.1 in panels (*a*), (*b*), (*c*), (*d*) and (*e*), respectively. (*f*) A transverse cut at $x/h = 1.7$ revealing the foliations of structures constituting the two branches of the mushroom-like vortex.

4.3.3. *Uncovering hidden structures*

We now focus on the region we highlighted in figure 16(*d*). The signature of a vortical structure is evident from the aFTLE landscape and it is corroborated by the isolines of an approximate first integral. Zooming in on the vicinity of this structure in figure 18, however, reveals the existence of another structure (see figure 20), showing no imprint on the aFTLE landscape.

To investigate this, we populate the neighbourhood around these two structures with 2-D cross-sections and compute the aFTLE field for each of them. At $x/h = 1$ (figure 20*a*), we note two mushroom-like pairs of structures, one larger and one smaller, but neither of the two display prominent closed regions that could signal a vortex. As we move towards larger x/h values, however, the aFTLE topography changes drastically. At $x/h = 1.4$ (figure 20*b*), the larger structure starts to fall apart before it completely disintegrates in the following cross-sections. In contrast, the smaller structure develops a salient closed loop, delineated by an aFTLE ridge, which is coincident with the largest of the reconstructed surfaces. In the next two cross-sections (figure 20*c*,*d*), the smaller of the two reconstructed surfaces comes into play as we further observe both parts of the vortex pair following closely the aFTLE ridges downstream. Finally, in the last cross-section (figure 20*e*), the vortex pair pattern is broken up in agreement with the reconstructed vortex pair coming to a halt.

This example epitomizes two notable features of Algorithm 1. First, using finer partitions results in the reconstruction of smaller structures consistent with the well-known hierarchy of coherent structures in turbulence. Second, this reconstruction takes place in an almost automated fashion with minimal reliance on user-defined parameters and with no need to advect trajectories of the barrier equation.

5. Conclusions

We have introduced a minimization principle to find an instantaneous approximate first integral of a given 3-D vector field. Level surfaces of this approximate first integral are expected to provide automated approximations to vortical streamsurfaces highlighting the instantaneous elliptic regions of the vector field. We have also proposed and tested a numerical algorithm for solving this minimization problem by means of total least squares and ridge regression. This algorithm has performed well on various solutions of the steady 3-D Euler equations on triply periodic and non-periodic domains. For steady velocity fields, the parametrized family of streamsurfaces rendered by our approach approximate elliptic (toroidal or cylindrical) LCSs without the need to advect a large number of trajectories required by Lagrangian methods (Haller *et al.* 2016). We have also illustrated on a 3-D junction flow the applicability of our algorithm for velocity fields defined as numerical datasets produced from computational fluid dynamics simulations.

We have additionally used the described algorithm to extract objectively defined instantaneous momentum transport barriers in a 3-D turbulent channel flow in an almost-automated fashion. Such barriers are streamsurfaces of an incompressible barrier equation defined by the Laplacian of the velocity field (Haller *et al.* 2020; Aksamit & Haller 2022). We have extracted vortical momentum transport barriers without the need to advect arrays of trajectories and found such barriers across multiple spatial scales.

The generality of the presented algorithm provides a fertile ground for its use in the visualization of the important features in a number of diverse applications. A straightforward example is the barrier equation derived by Haller *et al.* (2020) for the transport of vorticity. Furthermore, the purely Lagrangian approach of Haller *et al.* (2020) could be combined with our algorithm to produce LCSs for unsteady simulations. This method, unlike the instantaneous approach used for the production of supplementary movie 2, will yield smoothly varying structures that are also experimentally verifiable. Another application of our algorithm could be the visualization of the magnetic field resulting from magnetohydrodynamic turbulence simulations (Biskamp 2003). Future research can also apply the algorithm to direction fields like those emerging from studies of 3-D LCSs (Oettinger & Haller 2016), to 3-D material barriers to diffusive transport (Haller, Karrasch & Kogelbauer 2018) or to uncover LCSs acting as barriers in diverse applications (Martínez *et al.* 2021). Such studies could extend the automated extraction of 2-D LCSs and transport barriers (Katsanoulis & Haller 2019; Katsanoulis *et al.* 2020) to 3-D flows, facilitating their integration to numerical simulation codes.

Alternative solutions to the same optimization problem for an approximate first integral are certainly viable to investigate in future work. These could involve different basis functions (such as Chebyshev polynomials, wavelets or radial basis functions) instead of Fourier expansions. Techniques to mitigate the Gibbs phenomenon tied to non-periodic domains (Gegenbauer polynomials) (Gottlieb & Shu 1997) are also feasible to consider. Similarly, the effect of using Chebyshev nodes, instead of the uniform grids we considered here, to reduce the impact Runge's phenomenon has near the boundaries could be examined.

Supplementary movies. Supplementary movies are available at https://doi.org/10.1017/jfm.2022.992.

Funding. S.K. and G.H. acknowledge financial support from the Priority Program SPP 1881 (Turbulent Superstructures) of the German National Science Foundation (DFG). We are grateful to Dr D. Gatti for providing us with the 3-D turbulent channel flow dataset he originally generated as a benchmark case for the same program.

Declaration of interests. The authors report no conflict of interest.

Code and data availability. Example scripts generating the approximate first integral for the ABC flow are available at https://github.com/katsanoulis/Approximate_First_Integral/. The V-junction and turbulent channel flow datasets as well as their respective surface extraction scripts are available upon request from the first author.

Author ORCIDs.
Stergios Katsanoulis https://orcid.org/0000-0002-1186-5937;
Florian Kogelbauer https://orcid.org/0000-0002-6324-8084;
Roshan Kaundinya https://orcid.org/0000-0002-9916-6582;
Jesse Ault https://orcid.org/0000-0002-1232-362X;
George Haller https://orcid.org/0000-0003-1260-877X.

Appendix A. Typical flow visualization techniques

In this section, we apply classic vortex visualization methods in some of the flows for which we have constructed approximate first integrals. First, we test two isosurface-based criteria that are widely used in the literature to locate vortical structures, i.e. the λ_2-criterion of Jeong & Hussain (1995) and the Q-criterion of Hunt *et al.* (1988). Both of them are defined from the decomposition

$$\nabla \boldsymbol{v} = \boldsymbol{S} + \boldsymbol{\Omega}, \tag{A1}$$

where $\boldsymbol{S} = [\nabla \boldsymbol{v} + (\nabla \boldsymbol{v})^{\top}]/2$ is the rate-of-strain tensor and $\boldsymbol{\Omega} = [\nabla \boldsymbol{v} - (\nabla \boldsymbol{v})^{\top}]/2$ is the vorticity tensor.

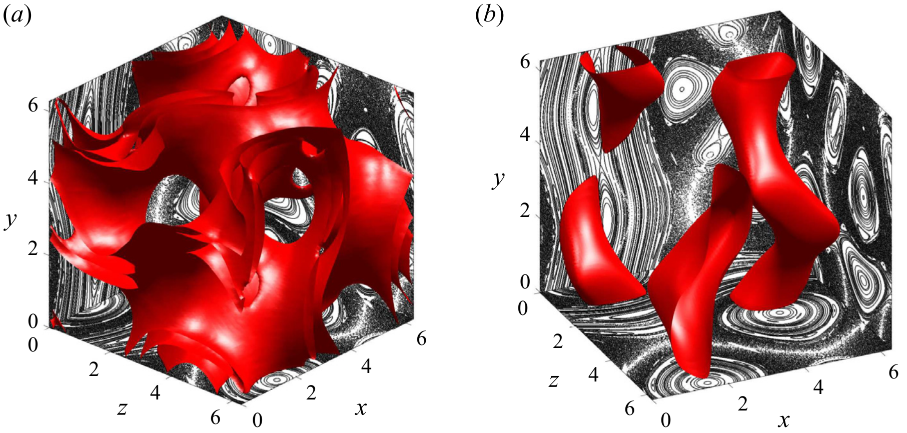

Figure 21. λ_2-criterion-based isosurfaces against Poincaré maps in the non-integrable ABC flow. The isosurfaces correspond to (*a*) $\lambda_2 = -0.02$ and (*b*) $\lambda_2 = -2.4$. The Poincaré maps are computed from a grid of 20×20 initial conditions on the $x = 0$, $y = 0$ and $z = 0$ planes running up to arclength 10^4.

According to the λ_2-criterion, vortical regions coincide with domains where

$$\lambda_2(\boldsymbol{S}^2 + \boldsymbol{\Omega}^2) < 0 \tag{A2}$$

with $\lambda_2(\boldsymbol{B})$ denoting the intermediate eigenvalue of the symmetric tensor $\boldsymbol{B}$. Similarly, the Q-criterion identifies vortical regions as those where

$$Q = \frac{1}{2}\left[\|\boldsymbol{\Omega}\|^2 - \|\boldsymbol{S}\|^2\right] > 0 \tag{A3}$$

with $\|\boldsymbol{B}\|$ denoting the Frobenius norm of $\boldsymbol{B}$.

We stress here that both of these criteria are only Galilean-invariant and, thus, depend on the frame of reference they are used on. Of equal importance is that, according to their definitions, they highlight vortical regions rather than surfaces. To bypass this, a specific value is usually chosen and the resulting isosurfaces are identified as the so-called vortices. Such a choice, however, would be justifiable, if the chosen isovalue was close to zero, as the original definitions postulated. Unfortunately, in typical flow visualizations, these isovalues are tuned to arbitrary values to match user expectations regarding the vortical features.

We highlight this in figure 21 using the λ_2-criterion for the non-integrable ABC flow. Specifically, we use one value close to zero (figure 21*a*) and one which corresponds to a drastically different topology for the resulting structures (figure 21*b*). We note that both of these values fail to capture even a single family of invariant tori. Indeed, the reconstructed surfaces tend to either have holes in the vicinity of the invariant tori (figure 21*a*) or be misaligned with the vortex cores (figure 21*b*). This is in stark contrast to the approximate-first-integral-based tori we have found in § 3.1.2.

A similar conclusion can be drawn for the flow inside the V-junction that we tested in § 3.4. Our approximate-first-integral algorithm correctly pinpoints the exact position of the recirculation bubbles in this flow. In contrast, we show in figure 22 the drastically different vortical features we obtain for different isovalues of the Q-criterion. Despite the four recirculation bubbles that are formed downstream, the isosurfaces based on the Q-criterion locate invariably two vortical features whose length also varies substantially for different Q values. What is even more remarkable is that such Q-criterion-based vortical features

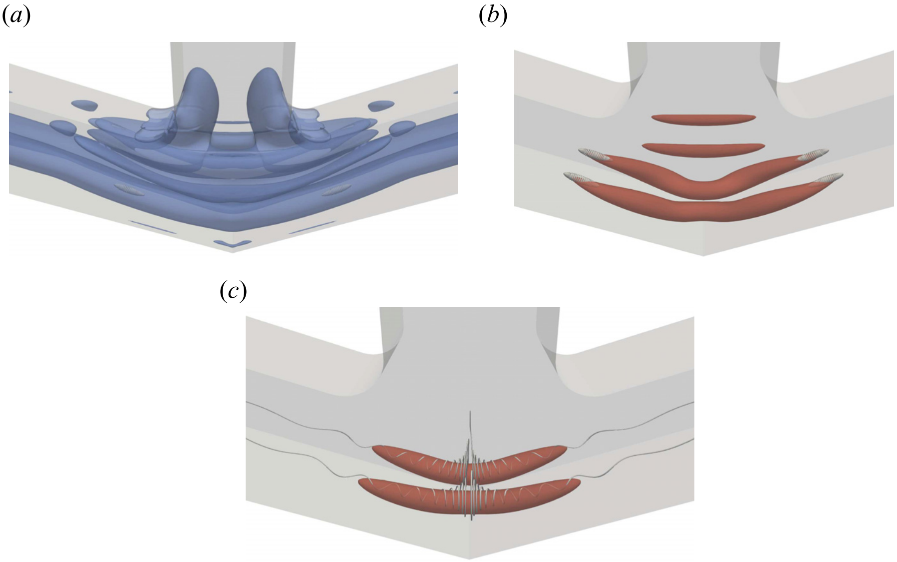

Figure 22. (*a*,*b*) Q-criterion-based isosurfaces against the recirculation bubbles for the flow inside the V-junction of § 3.4 ($Re = 230$). The isosurfaces correspond to (*a*) $Q = 0.02$ and (*b*) $Q = 50$. (*c*) Q-criterion-based isosurfaces for $Q = 50$ for a perturbed solution ($Re = 180$) where no recirculation bubbles are formed.

persist even for similar flows with slightly different Reynolds numbers that exhibit no fluid recirculation at all (see figure 22*c*). Importantly, our method finds no structure in the same spatial domain for these Reynolds numbers and hence correctly signals the lack of a recirculation bubble.

Finally, in figure 23(*a*,*b*), we present representative streamlines for the turbulent channel flow of § 4 based on the barrier field $\boldsymbol{\Delta v}(\boldsymbol{x})$, the velocity field $\boldsymbol{v}(\boldsymbol{x})$ in figure 23(*c*,*d*) and the vorticity field $\boldsymbol{\omega}(\boldsymbol{x})$ in figure 23(*e*,*f*) at time $t = 0$. For all three fields, we choose the same initial conditions, i.e. points that approximately lie on the ridge of the aFTLE field (computed based on the $\boldsymbol{\Delta v}(\boldsymbol{x})$ field) we identified in figure 20(*c*) at $x/h = 1.6$.

Based on these calculations, we draw the following conclusions. First, we observe the barrier streamlines being wrapped around the approximate-first-integral-based structure following even small protrusions on its surface like the one seen in figure 23(*a*). This structure is, thus, a correct approximation to an invariant manifold of the barrier field in agreement with the best-fit streamsurface of figure 24(*a*,*b*) as well as the aFTLE landscape of figure 20. For longer integration dummy times (figure 24*c*,*d*), however, we observe that this delineation of the barrier surface using streamlines quickly comes to a halt. Indeed, the streamlines fail to capture a significant portion of the barrier surface as x/h becomes larger, whereas for smaller x/h, they develop convoluted patterns that eventually fall apart resulting in elongated streamsurfaces that show no imprint on the aFTLE landscape. This constitutes the main reason why techniques aiming at the reconstruction of exact streamsurfaces through a better seed placement are not well suited for such flows.

Second, we note that the velocity streamlines form a misaligned (with respect to the extracted structure) tube that gives no indication of a vortical feature. Third, we remark that the vorticity streamlines correctly outline the outer shape of the mushroom-shaped structure imprinted on the aFTLE landscape without a detailed delineation, however, of the two branches that constitute it.

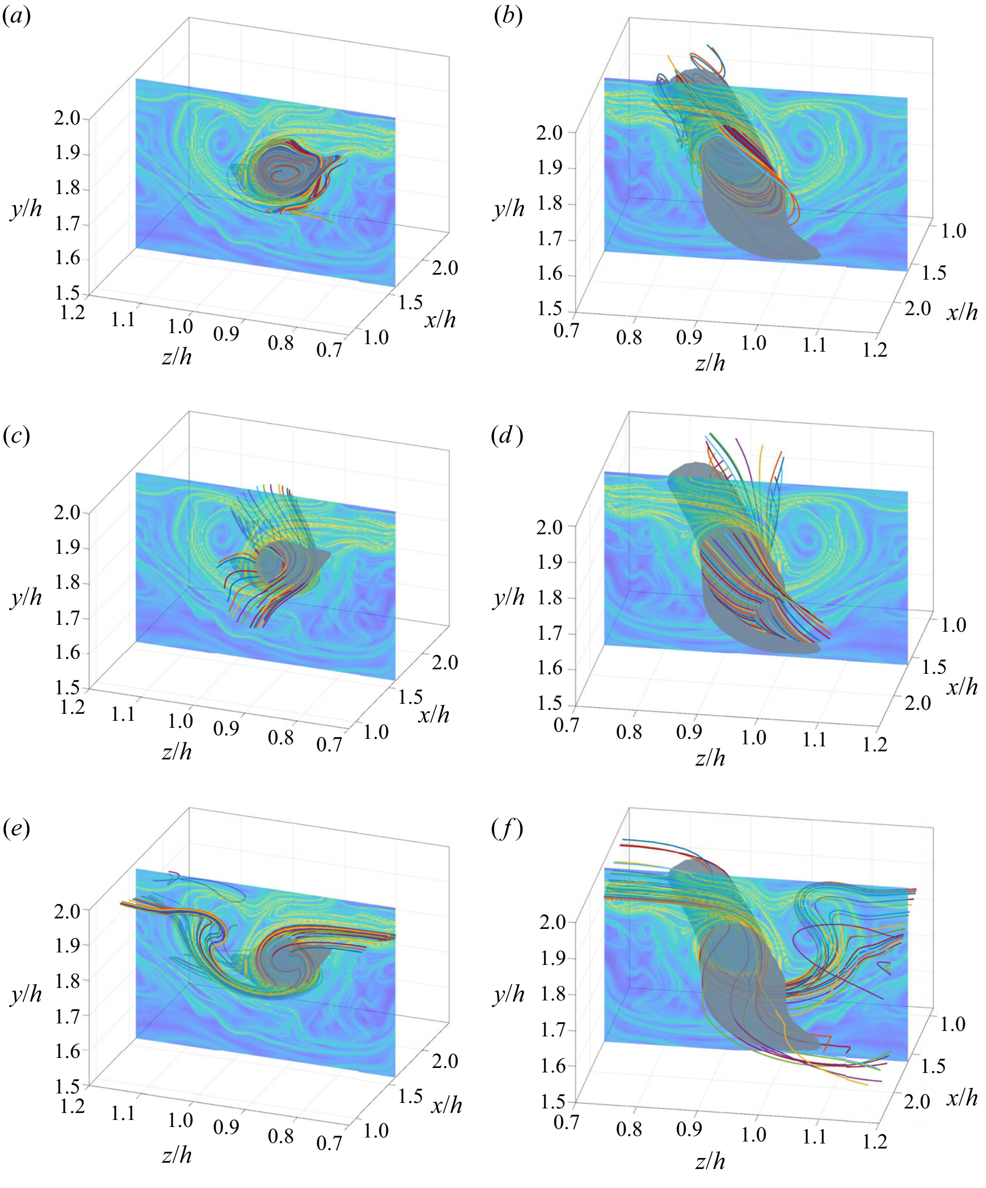

Figure 23. Streamlines of different vector fields emanating from points lying on the ridge of the aFTLE field at $x/h = 1.6$. Different views of streamlines of the (*a*,*b*) momentum barrier field, (*c*,*d*) velocity field and (*e*,*f*) vorticity field at $t = 0$.

Appendix B. Least squares for homogeneous systems

THEOREM B.1. *Let* $\boldsymbol{C} = \boldsymbol{U\Sigma V}^*$ *be the singular value decomposition of a matrix* $\boldsymbol{C}$*. Let, also,* $\boldsymbol{v}_1, \ldots, \boldsymbol{v}_k$ *be the last k columns of* $\boldsymbol{V}$ *whose corresponding singular values are equal to the smallest singular value* σ_1*. Then, all the linear combinations of the form*

$$\boldsymbol{x} = c_1\boldsymbol{v}_1 + \cdots + c_k\boldsymbol{v}_k \tag{B1}$$

with

$$c_1^2 + \cdots + c_k^2 = 1 \tag{B2}$$

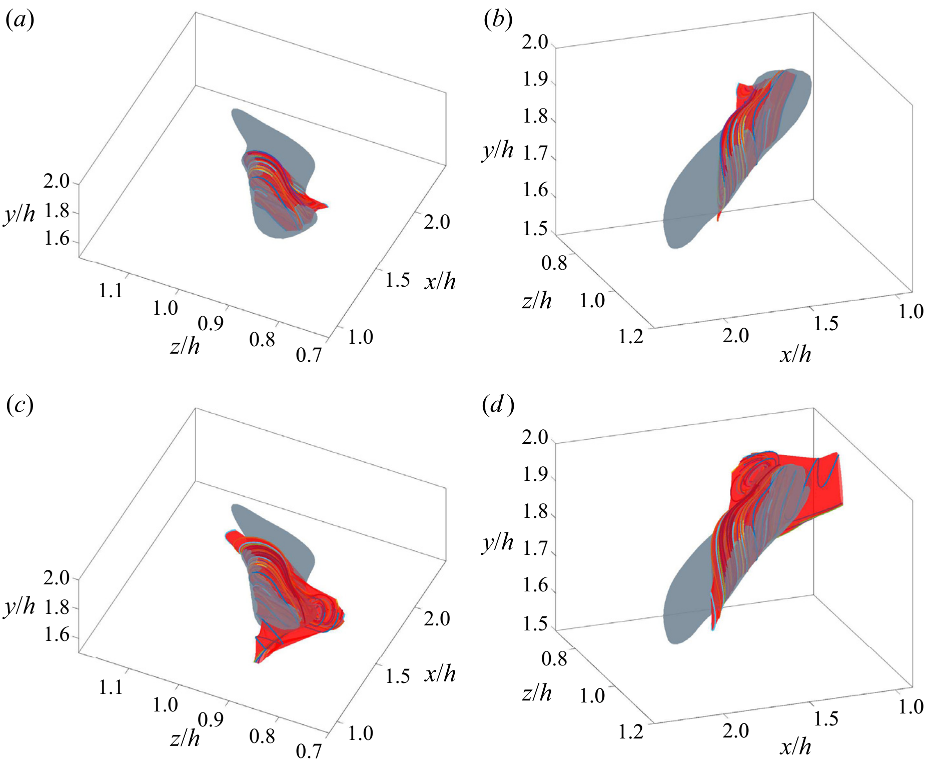

Figure 24. Different views of streamlines of the momentum barrier field originating from points lying on the ridge of the aFTLE field presented in figure 23. The integration in panels (*a*,*b*) and (*c*,*d*) corresponds to different dummy final times $s_{1,(a,b)}$ and $s_{1,(c,d)}$ with $s_{1,(a,b)} < s_{1,(c,d)}$. The best-fit streamsurfaces are depicted in red and are compared against the approximate-first-integral-based structure in grey.

are unit-norm least-squares solutions to the homogeneous system

$$\boldsymbol{C}\boldsymbol{x} = \boldsymbol{0}. \tag{B3}$$

Proof. We want to find the solution $\boldsymbol{x}$ with $|\boldsymbol{x}| = 1$ that minimizes $|\boldsymbol{C}\boldsymbol{x}|$ or $|\boldsymbol{U}\boldsymbol{\Sigma}\boldsymbol{V}^*\boldsymbol{x}|$. Because $\boldsymbol{U}$ is unitary and, thus, acts as an isometry, this is equivalent to minimizing $|\boldsymbol{\Sigma}\boldsymbol{V}^*\boldsymbol{x}|$ or $|\boldsymbol{\Sigma}\boldsymbol{y}|$ with $\boldsymbol{y} = \boldsymbol{V}^*\boldsymbol{x}$. Here, $\boldsymbol{V}$ is also unitary, so $|\boldsymbol{y}| = 1$ is equivalent to $|\boldsymbol{x}| = 1$. Therefore we want the unit-norm vector $\boldsymbol{y}$ that minimizes $|\boldsymbol{\Sigma}\boldsymbol{y}|$, i.e. the quantity

$$\sigma_1^2 y_1^2 + \cdots + \sigma_n^2 y_n^2. \tag{B4}$$

By the definition of SVD, we have

$$\left.\begin{array}{c} \sigma_1 \geq \sigma_1 \Leftrightarrow \sigma_1^2 \geq \sigma_1^2 \\ \vdots \\ \sigma_n \geq \sigma_1 \Leftrightarrow \sigma_n^2 \geq \sigma_1^2 \end{array}\right\} \Leftrightarrow \left.\begin{array}{c} \sigma_1^2 y_1^2 \geq \sigma_1^2 y_1^2 \\ \vdots \\ \sigma_n^2 y_n^2 \geq \sigma_1^2 y_n^2 \end{array}\right\} \tag{B5}$$

and after summing up all the inequalities, we obtain

$$\sigma_1^2 y_1^2 + \sigma_2^2 y_2^2 + \cdots + \sigma_n^2 y_n^2 \geq \left(y_1^2 + y_2^2 + \cdots + y_n^2\right)\sigma_1^2 = \sigma_1^2, \tag{B6}$$

with the equality holding if

$$y_{n-k+1} = y_{n-k+2} = \cdots = y_n = 0. \tag{B7}$$

We then have $\boldsymbol{x} = \boldsymbol{V}\boldsymbol{y} = y_1\boldsymbol{v}_1 + \cdots + y_n\boldsymbol{v}_n$ and, thus, (B7) is equivalent to

$$\boldsymbol{x} = c_1\boldsymbol{v}_1 + \cdots + c_k\boldsymbol{v}_k \tag{B8}$$

with $c_1 = y_1, \ldots, c_k = y_k$ and $c_1^2 + \cdots + c_k^2 = 1$. ■

Appendix C. Solving for H after imposing the real constraint

We define a complex vector $\boldsymbol{h} \in \mathbb{C}^n$, where n represents the number of vectors $\boldsymbol{k} \in \mathbb{Z}^3$ such that $|\boldsymbol{k}| \leq N$ and we also represent the individual entries of $\boldsymbol{h}$ as $h_{\boldsymbol{k}}$. Further, in conjunction with § 2, we define a $m \times n$ matrix, where m represents the total number of grid points. We are interested in minimizing $\boldsymbol{h}^*\boldsymbol{C}^*\boldsymbol{C}\boldsymbol{h}$ subject to the constraints $\boldsymbol{h}^*\boldsymbol{h} = 1$ and $h_{-\boldsymbol{k}} = h_{\boldsymbol{k}}^*$. The second constraint is not natural to solve using known optimization techniques, due to which we will modify the above problem rearranging $\boldsymbol{h}$ as a vector in $\mathbb{R}^{2n}$.

Naively, one can construct a column vector with first n real entries of $\boldsymbol{h}$ followed by their corresponding imaginary entries

$$\boldsymbol{v} = \begin{pmatrix} \mathrm{Re}(\boldsymbol{h}) \\ \mathrm{Im}(\boldsymbol{h}) \end{pmatrix}. \tag{C1}$$

Similarly, one can reorganize $\boldsymbol{A} = \boldsymbol{C}^*\boldsymbol{C}$ and obtain

$$\boldsymbol{D} = \begin{bmatrix} \boldsymbol{A}_r & -\boldsymbol{A}_{\mathrm{i}} \\ \boldsymbol{A}_{\mathrm{i}} & \boldsymbol{A}_r \end{bmatrix}, \tag{C2}$$

where $\boldsymbol{A}_r = (\boldsymbol{A} + \boldsymbol{A}^{\mathrm{T}})/2$ and $\boldsymbol{A}_{\mathrm{i}} = (\boldsymbol{A} - \boldsymbol{A}^{\mathrm{T}})/2\mathrm{i}$. Thus, we have $\boldsymbol{v}^{\mathrm{T}}\boldsymbol{D}\boldsymbol{v} = \boldsymbol{h}^*\boldsymbol{A}\boldsymbol{h}$ subject to the constraints $\boldsymbol{v}^{\mathrm{T}}\boldsymbol{v} = \boldsymbol{h}^*\boldsymbol{h} = 1$ and $\boldsymbol{U}\boldsymbol{v} = 0$. In our case, $\boldsymbol{U}$ is a matrix of the form

$$\boldsymbol{U} = \left[\boldsymbol{K}_{(n\times n)} \quad \boldsymbol{J}_{(n\times n)}\right]_{n\times 2n} \tag{C3}$$

$$K_{ij} = \begin{cases} 1 & i=j, i<n/2, j<n/2 \\ -1 & i=n/2+j, i<n/2, j<n/2 \\ 0 & \end{cases} \Bigg| J_{ij} = \begin{cases} 1 & i=j, i<n/2, j<n/2 \\ 1 & i=n/2+j, i<n/2, j<n/2 \\ 0 & \end{cases} \tag{C4}$$

The above optimization problem has a solution by Golub (1973). We state a form of the theorem that will be useful for us.

THEOREM C.1. *Minimizing* $\boldsymbol{v}^T\boldsymbol{D}\boldsymbol{v}$ *subject to* $\boldsymbol{v}^T\boldsymbol{v} = 1$, $\boldsymbol{U}\boldsymbol{v} = 0$, *where* $\boldsymbol{v} \in \mathbb{R}^{2n}$ *is equivalent to minimizing* $\boldsymbol{l}^T\boldsymbol{E}\boldsymbol{l}$ *subject to* $\boldsymbol{l}^T\boldsymbol{l} = 1$, *where* $\boldsymbol{l} \in \mathbb{R}^n$ *provided* $\boldsymbol{U}$ *is a* $n \times 2n$ *matrix.*

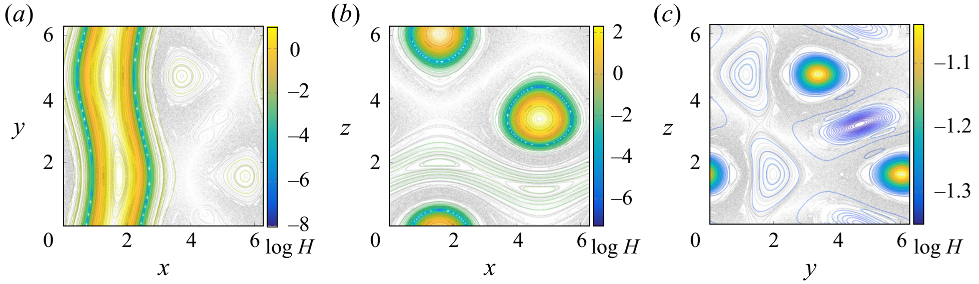

Figure 25. Analysis of the non-integrable ABC flow using a computational grid of 100^3 points and 9170 Fourier modes after constraining H to be a real scalar field. Level sets of the reconstructed first integral at (*a*) $z = 0$, (*b*) $y = 0$ and (*c*) $x = 0$. The Poincaré map is overlaid on each section based on a uniform grid of 20×20 initial conditions.

Proof. Following Golub (1973), we can write

$$\boldsymbol{U}^{\mathrm{T}} = \boldsymbol{QR} = \boldsymbol{Q}_{2n\times 2n}\begin{bmatrix}\boldsymbol{R}'_{n\times n}\\ \boldsymbol{0}_{n\times n}\end{bmatrix}_{2n\times n}, \tag{C5}$$

where $\boldsymbol{Q}$ is an orthogonal matrix and $\boldsymbol{R}'$ is an upper triangular matrix. The constraint then reads

$$\boldsymbol{R}^{\mathrm{T}}\boldsymbol{Q}^{\mathrm{T}}\boldsymbol{v} = 0, \tag{C6}$$

$$\boldsymbol{R}^{\mathrm{T}}\boldsymbol{v}_Q = 0. \tag{C7}$$

The vector $\boldsymbol{v}_Q = \begin{bmatrix}\boldsymbol{0}_{n\times 1}\\ \boldsymbol{l}_{n\times 1}\end{bmatrix}$ is a solution to the above constraint. Expressing the objective function in terms of $\boldsymbol{v}_Q$, we have

$$\boldsymbol{v}^{\mathrm{T}}\boldsymbol{D}\boldsymbol{v} = \boldsymbol{v}^{\mathrm{T}}\boldsymbol{Q}\boldsymbol{Q}^{-1}\boldsymbol{D}(\boldsymbol{Q}^{-1})^{\mathrm{T}}\boldsymbol{Q}^{\mathrm{T}}\boldsymbol{v} = \boldsymbol{v}_Q^{\mathrm{T}}\begin{bmatrix}(\boldsymbol{Q}^{\mathrm{T}}\boldsymbol{DQ})_{11} & (\boldsymbol{Q}^{\mathrm{T}}\boldsymbol{DQ})_{12}\\ (\boldsymbol{Q}^{\mathrm{T}}\boldsymbol{DQ})_{21} & (\boldsymbol{Q}^{\mathrm{T}}\boldsymbol{DQ})_{22}\end{bmatrix}\boldsymbol{v}_Q = \boldsymbol{l}^{\mathrm{T}}\boldsymbol{El} \tag{C8}$$

subject to the constraint $\boldsymbol{l}^{\mathrm{T}}\boldsymbol{l} = 1$ with $\boldsymbol{E} = (\boldsymbol{Q}^{\mathrm{T}}\boldsymbol{DQ})_{22}$. ■

Using this theorem, we can see that the eigenvector of $\boldsymbol{E}$ corresponding to the minimum eigenvalue would be the solution (since $\boldsymbol{E}$ is a symmetric matrix). The vector of interest $\boldsymbol{h}$ can be reconstructed as follows:

$$\boldsymbol{h} = [\boldsymbol{Q}(\boldsymbol{v}_Q)_{min}]_1 + \mathrm{i}[\boldsymbol{Q}(\boldsymbol{v}_Q)_{min}]_2,\ \boldsymbol{Q}(\boldsymbol{v}_Q)_{min} = \begin{pmatrix}\{[\boldsymbol{Q}(\boldsymbol{v}_Q)_{min}]_1\}_{n\times 1}\\ \{[\boldsymbol{Q}(\boldsymbol{v}_Q)_{min}]_2\}_{n\times 1}\end{pmatrix}. \tag{C9}$$

The results of this solution method for the non-integrable ABC flow on three different planes are depicted in figure 25. Again, we note the very good agreement of the reconstructed level sets with both the Poincaré maps and the level sets of figure 3.

Appendix D. Efficient computation of SVD for tall-skinny matrices

Let $\boldsymbol{C}$ be an $m \times n$ matrix with $m \gg n$. To make use of the tall-thin structure of this matrix, we follow an approach similar to the one described by Schmidt (2020) and factor

$$\boldsymbol{C}_{m\times n} = \boldsymbol{Q}_{m\times n}\boldsymbol{R}_{n\times n} \tag{D1}$$

using the so-called thin QR factorization of $\boldsymbol{C}$. The SVD of $\boldsymbol{R}$ gives

$$\boldsymbol{C} = \boldsymbol{QR} = \boldsymbol{Q}(\boldsymbol{U}_R\boldsymbol{\Sigma}_R\boldsymbol{V}_R^{\mathrm{T}}) = (\boldsymbol{QU}_R)\boldsymbol{\Sigma}_R\boldsymbol{V}_R^{\mathrm{T}}. \tag{D2}$$

This is in turn a singular value decomposition of $\boldsymbol{C}$ because $\boldsymbol{QU}_R$ is unitary as the product of unitary matrices. To avail ourselves of this result, we can split $\boldsymbol{C} = \left[\begin{smallmatrix} C_1 \\ C_2 \end{smallmatrix}\right]$, followed by $\boldsymbol{C}_i = \boldsymbol{Q}_i\boldsymbol{R}_i$ $(i = 1, 2)$ and, thus, we obtain

$$\boldsymbol{C} = \begin{bmatrix} \boldsymbol{Q}_1 & 0 \\ 0 & \boldsymbol{Q}_2 \end{bmatrix} \begin{bmatrix} \boldsymbol{R}_1 \\ \boldsymbol{R}_2 \end{bmatrix}. \tag{D3}$$

This is not yet a QR factorization of $\boldsymbol{C}$ as the right factor is not upper triangular. We then perform another thin QR factorization on $\left[\begin{smallmatrix} \boldsymbol{R}_1 \\ \boldsymbol{R}_2 \end{smallmatrix}\right]$ and obtain

$$\boldsymbol{C} = \begin{bmatrix} \boldsymbol{Q}_1 & 0 \\ 0 & \boldsymbol{Q}_2 \end{bmatrix} \boldsymbol{QR}, \tag{D4}$$

which is a QR factorization of $\boldsymbol{C}$. Based on that, we can partition the original computation domain into smaller sub-domains, compute the $\boldsymbol{R}_i$ matrices for each of them, combine these to produce the final $\boldsymbol{R}$ matrix as in (D4) and, finally, run SVD on this $n \times n$ matrix. This procedure is readily parallelizable.

For the purposes of our computation described in § 3.1.2, we used 10 cores on the Euler cluster of ETH Zurich and within each core, we chose 5 more partitions. This resulted in approximately the same memory footprint as for the solution of the eigenvalue problem. If the memory is not enough, the number of partitions can be increased with a subsequent increase in the computational time.

Appendix E. A different solution to the optimization problem

Let us assume that we start by fixing the Fourier coefficient of particular modes. To avoid inducing unnecessary inhomogeneity to our solution, we are going to set $\hat{H}_{\boldsymbol{k}} = 1$ for $\boldsymbol{k} = (1, 0, 0)$, $\boldsymbol{k} = (0, 1, 0)$, $\boldsymbol{k} = (0, 0, 1)$. Similarly, we impose $\hat{H}_{-\boldsymbol{k}} = \hat{H}^*_{\boldsymbol{k}} = 1$. We further denote by

$$\begin{aligned} \mathcal{K} = \{\boldsymbol{k} | \boldsymbol{k} \in \mathbb{Z}^3 \wedge |\boldsymbol{k}| \leq N \wedge \boldsymbol{k} \neq (1, 0, 0) \wedge \boldsymbol{k} \neq (-1, 0, 0) \wedge \boldsymbol{k} \neq (0, 1, 0) \\ \wedge \boldsymbol{k} \neq (0, -1, 0) \wedge \boldsymbol{k} \neq (0, 0, 1) \wedge \boldsymbol{k} \neq (0, 0, -1)\} \end{aligned} \tag{E1}$$

the set of the remaining Fourier modes. Then, the invariance condition reads

$$\boldsymbol{Ch} = \boldsymbol{b}, \tag{E2}$$

where $C_{ij} = \exp(\mathrm{i}\boldsymbol{k}_j \cdot \boldsymbol{x}_i)\boldsymbol{k}_j \cdot \boldsymbol{v}_i$, $\boldsymbol{h} = \{\hat{H}_{\boldsymbol{k}} | \boldsymbol{k} \in \mathbb{Z}^3 \wedge \boldsymbol{k} \in \mathcal{K}\}$ and $\boldsymbol{b} = [b_1 \quad b_2 \quad \cdots \quad b_l \quad \cdots \quad b_m]^{\mathrm{T}}$ with

$$b_l = -2\mathrm{i}\left(\sin x v_x + \sin y v_y + \sin z v_z\right). \tag{E3}$$

Essentially, what we have attained here is to transform the homogeneous system of equations to an inhomogeneous one for which we can now use ordinary least squares or

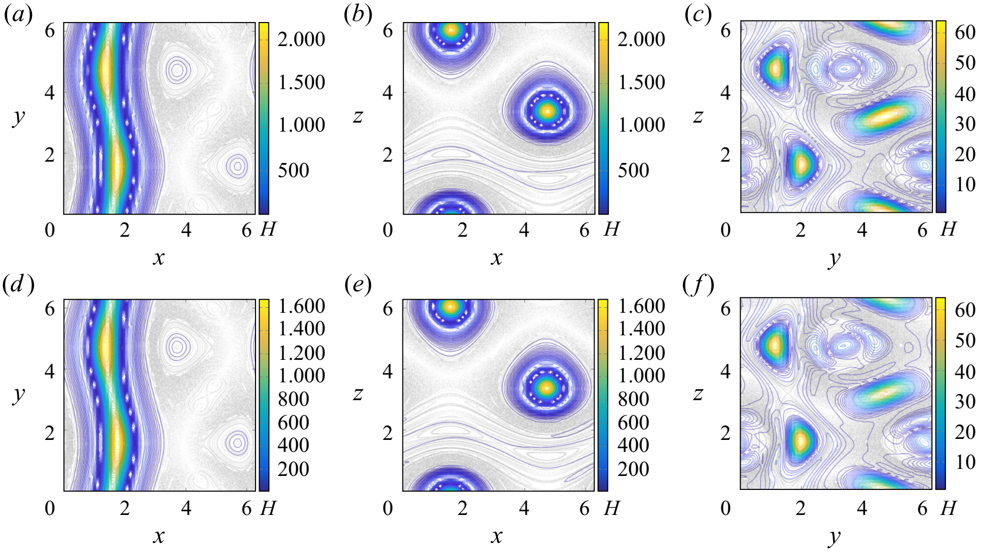

Figure 26. Analysis of the non-integrable ABC flow using a computational grid of 60^3 points and 9170 Fourier modes. Level sets of the reconstructed first integral at (*a*,*d*) $z = 0$, (*b*,*e*) $y = 0$ and (*c*,*f*) $x = 0$. Panels (*a*–*c*) are constructed using ordinary least squares, whereas panels (*d*–*f*) are generated using ridge regression. The Poincaré map is overlaid on each section based on a uniform grid of 20 × 20 initial conditions.

ridge regression. The ridge-regression solution is given as

$$\hat{\boldsymbol{h}} = \boldsymbol{V}\left(\boldsymbol{\Sigma}^{\top}\boldsymbol{\Sigma} + \lambda \boldsymbol{I}\right)^{-1}\boldsymbol{\Sigma}^{\top}\boldsymbol{U}^{*}\boldsymbol{b}, \tag{E4}$$

whereas for $\lambda = 0$, we obtain the ordinary least-squares solution. This expression shows that the trick we employed in the homogeneous case with the QR decomposition cannot be applied here given that the solution depends on the explicit construction of $\boldsymbol{U}$. We are, therefore, limited with regard to the maximum size of the computational grid we can use before we run into memory issues.

Nonetheless, in figure 26, we provide the two solutions for the non-integrable ABC flow using 60 points per direction and the same number of Fourier modes as before. For the ridge regression, we used cross-validation and kept the solution with the smallest least-squares error out of the solutions generated for $\lambda \in \{1, 10^{-1}, 10^{-2}, 10^{-3}, 10^{-4}\}$. The results appear to be inferior to the homogeneous-system-based solutions suggesting that this approach is recommended only for numerical datasets defined over smaller grids.

REFERENCES

AKSAMIT, N.O. & HALLER, G. 2022 Objective momentum barriers in wall turbulence. *J. Fluid Mech.* **941**, A3.

ANTUONO, M. 2020 Tri-periodic fully three-dimensional analytic solutions for the Navier–Stokes equations. *J. Fluid Mech.* **890**, A23.

ARNOLD, V.I. 1989 *Mathematical Methods of Classical Mechanics*. Springer.

ARNOLD, V.I. & KHESIN, B.A. 1999 *Topological Methods in Hydrodynamics*, vol. 125. Springer Science & Business Media.

AULT, J.T., FANI, A., CHEN, K.K., SHIN, S., GALLAIRE, F. & STONE, H.A. 2016 Vortex-breakdown-induced particle capture in branching junctions. *Phys. Rev. Lett.* **117** (8), 084501.

BATCHELOR, G.K. 2000 *An Introduction to Fluid Dynamics*. Cambridge University Press.

BISKAMP, D. 2003 *Magnetohydrodynamic Turbulence*. Cambridge University Press

BLAZEVSKI, D. & HALLER, G. 2014 Hyperbolic and elliptic transport barriers in three-dimensional unsteady flows. *Physica* D **273**, 46–62.

BORN, S., WIEBEL, A., FRIEDRICH, J., SCHEUERMANN, G. & BARTZ, D. 2010 Illustrative stream surfaces. *IEEE Trans. Vis. Comput. Graph.* **16** (6), 1329–1338.

CARR, H., SNOEYINK, J. & AXEN, U. 2003 Computing contour trees in all dimensions. *Comput. Geom.* **24** (2), 75–94.

CHENG, C.Q. & SUN, Y.S. 1989 Existence of invariant tori in three-dimensional measure-preserving mappings. *Celestial Mech. Dyn. Astron.* **47**, 275–292.

CHERN, A., KNÖPPEL, F., PINKALL, U. & SCHRÖDER, P. 2017 Inside fluids: clebsch maps for visualization and processing. *ACM Trans. Graph.* **36** (4), 1–11.

CHIERCHIA, L. & GALLAVOTTI, G. 1982 Smooth prime integrals for quasi-integrable Hamiltonian systems. *Il Nuovo Cimento* B **67**, 277–295.

CHONG, M.S., PERRY, A.E. & CANTWELL, B.J. 1990 A general classification of three-dimensional flow fields. *Phys. Fluids* A*: Fluid Dyn.* **2** (5), 765–777.

DOMBRE, T., FRISCH, U., GREENE, J.M., HÉNON, M., MEHR, A. & SOWARD, A.M. 1986 Chaotic streamlines in the ABC flows. *J. Fluid Mech.* **167**, 353–391.

GOLUB, G.H. 1973 Some modified matrix eigenvalue problems. *SIAM Rev.* **15** (2), 318–334.

GOLUB, G.H. & PEREYRA, V. 1973 The differentiation of pseudo-inverses and nonlinear least squares problems whose variables separate. *SIAM J. Numer. Anal.* **10** (2), 413–432.

GOTTLIEB, D. & SHU, C.-W. 1997 On the Gibbs phenomenon and its resolution. *SIAM Rev.* **39** (4), 644–668.

HALLER, G. 2005 An objective definition of a vortex. *J. Fluid Mech.* **525**, 1–26.

HALLER, G. 2015 Lagrangian coherent structures. *Annu. Rev. Fluid Mech.* **47**, 137–162.

HALLER, G. 2021 Can vortex criteria be objectivized? *J. Fluid Mech.* **908**, A25.

HALLER, G., HADJIGHASEM, A., FARAZMAND, M. & HUHN, F. 2016 Defining coherent vortices objectively from the vorticity. *J. Fluid Mech.* **795**, 136–173.

HALLER, G., KARRASCH, D. & KOGELBAUER, F. 2018 Material barriers to diffusive and stochastic transport. *Proc. Natl Acad. Sci.* **115** (37), 9074–9079.

HALLER, G., KATSANOULIS, S., HOLZNER, M., FROHNAPFEL, B. & GATTI, D. 2020 Objective barriers to the transport of dynamically active vector fields. *J. Fluid Mech.* **905**, A17.

HALLER, G. & MEZIĆ, I. 1998 Reduction of three-dimensional, volume-preserving flows with symmetry. *Nonlinearity* **11** (2), 319–339.

HENON, M. 1966 Sur la topologie des lignes de courant dans un cas particulier. *C. R. Acad. Sci. Paris A* **262**, 312–314.

HILL, M.J.M. 1894 On a spherical vortex. *Phil. Trans. R. Soc.* A **185**, 213–245.

HOLMES, P. 1984 Some remarks on chaotic particle paths in time-periodic, three-dimensional swirling flows. *Contemp. Maths* **28**, 393–404.

HULTQUIST, J.P.M. 1992 Constructing stream surfaces in steady 3D vector fields. In *Proceedings Visualization '92*, pp. 171–178. IEE Computer Society Press.

HUNT, J.C.R., WRAY, A. & MOIN, P. 1988 Eddies, stream, and convergence zones in turbulent flows. Center for turbulence research report CTR-S88, pp. 193–208.

JEONG, J. & HUSSAIN, F. 1995 On the identification of a vortex. *J. Fluid Mech.* **285**, 69–94.

KATSANOULIS, S., FARAZMAND, M., SERRA, M. & HALLER, G. 2020 Vortex boundaries as barriers to diffusive vorticity transport in two-dimensional flows. *Phys. Rev. Fluids* **5** (2), 024701.

KATSANOULIS, S. & HALLER, G. 2019 BarrierTool Manual. Retrieved from https://github.com/LCSETH.

KIM, J., MOIN, P. & MOSER, R. 1987 Turbulence statistics in fully developed channel flow at low Reynolds number. *J. Fluid Mech.* **177**, 133–166.

LLIBRE, J. & VALLS, C. 2012 A note on the first integrals of the ABC system. *J. Math. Phys.* **53** (2), 023505.

LORENSEN, W.E. & CLINE, H.E. 1987 Marching cubes: a high resolution 3d surface construction algorithm. *SIGGRAPH* **21** (4), 163–169.

MARTÍNEZ, L., *et al.* 2021 Metal-catalyst-free gas-phase synthesis of long-chain hydrocarbons. *Nat. Commun.* **12**, 5937.

MARTINEZ–ESTURO, J., SCHULZE, M., RÖSSL, C. & THEISEL, H. 2013 Global selection of stream surfaces. *Comput. Graph. Forum (Proc. Eurograph.)* **32** (2), 113–122.

OETTINGER, D., AULT, J.T., STONE, H.A. & HALLER, G. 2018 Invisible anchors trap particles in branching junctions. *Phys. Rev. Lett.* **121** (5), 054502.

OETTINGER, D., BLAZEVSKI, D. & HALLER, G. 2016 Global variational approach to elliptic transport barriers in three dimensions. *Chaos* **26** (3), 033114.

OETTINGER, D. & HALLER, G. 2016 An autonomous dynamical system captures all lcss in three-dimensional unsteady flows. *Chaos* **26** (10), 103111.

PÖSCHEL, J. 1982 Integrability of Hamiltonian systems on cantor sets. *Commun. Pure Appl. Maths* **35**, 653–696.

PEIKERT, R. & SADLO, F. 2007 Visualization methods for vortex rings and vortex breakdown bubbles. In *Proceedings of the 9th Joint Eurographics/IEEE VGTC conference on Visualization* (ed. K. Museth, T. Moeller & A. Ynnerman), pp. 211–218. The Eurographics Association.

PEIKERT, R. & SADLO, F. 2009 Topologically relevant stream surfaces for flow visualization. In *Proceedings of the 25th Spring Conference on Computer Graphics*, pp. 35–42. Association for Computing Machinery.

PENG, N. & YANG, Y. 2018 Effects of the Mach number on the evolution of vortex-surface fields in compressible Taylor–Green flows. *Phys. Rev. Fluids* **3** (1), 013401.

PULLIN, D.I. & YANG, Y. 2014 Whither vortex tubes? *Fluid Dyn. Res.* **46** (6), 061418.

ROBINSON, S.K. 1991 Coherent motions in the turbulent boundary layer. *Annu. Rev. Fluid Mech.* **23** (1), 601–639.

SADLO, F. & PEIKERT, R. 2007 Efficient visualization of Lagrangian coherent structures by filtered AMR ridge extraction. *IEEE Trans. Vis. Comput. Graph.* **13** (6), 1456–1463.

SCHMIDT, D. 2020 A survey of Singular Value Decomposition methods for distributed tall/skinny data. In *2020 IEEE/ACM 11th Workshop on Latest Advances in Scalable Algorithms for Large-Scale Systems (ScalA)*, pp. 27–34. IEEE.

SCHULZE, M., MARTINEZ-ESTURO, J., GÜNTHER, T., RÓSSL, C., SEIDEL, H.-P., WEINKAUF, T. & THEISEL, H. 2014 Sets of globally optimal stream surfaces for flow visualization. *Comput. Graph. Forum (Proc. EuroVis)* **33** (3), 1–10.

SHIN, S., AULT, J. & STONE, H. 2015 Flow-driven rapid vesicle fusion via vortex trapping. *Langmuir* **31** (26), 7178–7182.

SOTIROPOULOS, F., VENTIKOS, Y. & LACKEY, T. 2001 Chaotic advection in three-dimensional stationary vortex-breakdown bubbles: Šil'nikov's chaos and the devil's staircase. *J. Fluid Mech.* **444**, 257–297.

VAN WIJK, J.J. 1993 Implicit stream surfaces. In *Proceedings Visualization'93*, pp. 245–252. IEEE.

VIGOLO, D., RADL, S. & STONE, H.A. 2014 Unexpected trapping of particles at a T junction. *Proc. Natl Acad. Sci.* **111** (13), 4770–4775.

WELLER, H.G., TABOR, G., JASAK, H. & FUREBY, C. 1998 A tensorial approach to computational continuum mechanics using object-oriented techniques. *Comput. Phys.* **12** (6), 620–631.

XIONG, S. & YANG, Y. 2017 The boundary-constraint method for constructing vortex-surface fields. *J. Comput. Phys.* **339**, 31–45.

XIONG, S. & YANG, Y. 2019 Identifying the tangle of vortex tubes in homogeneous isotropic turbulence. *J. Fluid Mech.* **874**, 952–978.

YANG, Y. & PULLIN, D.I. 2010 On Lagrangian and vortex-surface fields for flows with Taylor–Green and Kida–Pelz initial conditions. *J. Fluid Mech.* **661**, 446–481.

YANG, Y. & PULLIN, D.I. 2011 Evolution of vortex-surface fields in viscous Taylor–Green and Kida–Pelz flows. *J. Fluid Mech.* **685**, 146–164.

ZHAO, Y., YANG, Y. & CHEN, S. 2016*a* Evolution of material surfaces in the temporal transition in channel flow. *J. Fluid Mech.* **793**, 840–876.

ZHAO, Y., YANG, Y. & CHEN, S. 2016*b* Vortex reconnection in the late transition in channel flow. *J. Fluid Mech.* **802**, R4.

ZHOU, J., ADRIAN, R.J., BALACHANDAR, S. & KENDALL, T.M. 1999 Mechanisms for generating coherent packets of hairpin vortices in channel flow. *J. Fluid Mech.* **387**, 353–396.

ZIGLIN, S.L. 1988 Splitting of the separatrices and the nonexistence of first integrals in systems of differential equations of Hamiltonian type with two degrees of freedom. *Maths USSR-Izvestiya* **31** (2), 407.

ZIGLIN, S.L. 1998 On the absence of a real-analytic first integral for ABC flow when A = B. *Chaos* **8** (1), 272–273.